

Ensemble Representation of Satellite Precipitation Uncertainty using an Uncalibrated, Nonstationary, Anisotropic Autocorrelation Model

Samantha H. Hartke¹, Daniel Benjamin Wright¹, Zhe Li², Viviana Maggioni³, Dalia Kirschbaum⁴, and Sana Khan⁵

¹University of Wisconsin-Madison

²Colorado State University

³George Mason University

⁴NASA Goddard Space Flight Center

⁵NASA Goddard Space Flight Center, and Earth System Science Interdisciplinary Center, University of Maryland

November 21, 2022

Abstract

The usefulness of satellite multi-sensor precipitation (SMP) and other satellite-informed precipitation products in water resources modeling can be hindered by substantial errors which vary considerably with spatiotemporal scale. One approach to cope with these errors is by combining SMPs with ensemble generation methods, such that each ensemble member reflects one plausible realization of the true—but unknown—precipitation. This requires replicating the spatiotemporal autocorrelation structure of SMP errors. The climatology of this structure is unknown for most locations due to a lack of ground reference observations, while the unique anisotropy and nonstationarity within any particular precipitation system limit the relevance of this climatology to the depiction of error in individual storm systems. Characterizing and simulating this autocorrelation across spatiotemporal scales has thus been called a grand challenge within the precipitation community. We introduce the Space-Time Rainfall Error and Autocorrelation Model (STREAM), which combines anisotropic and nonstationary SMP spatiotemporal correlation structures with a pixel-scale precipitation error model to stochastically generate ensemble precipitation fields that resemble “ground truth” precipitation. We generate STREAM precipitation ensembles at high resolution (1-hour, 0.1°) with minimal reliance on ground-reference data, and evaluate these ensembles at multiple scales. STREAM ensembles consistently “bracket” ground-truth observations and replicate the autocorrelation structure of ground-truth precipitation fields. STREAM is compatible with pixel-scale error/uncertainty formulations beyond those presented here, and could be applied globally to other precipitation sources such as numerical weather predictions or “blended” products. In combination with recent work in SMP uncertainty characterization, STREAM could be run without any ground data.

Hosted file

stream.supportinginfo.docx available at <https://authorea.com/users/529616/articles/597144-ensemble-representation-of-satellite-precipitation-uncertainty-using-an-uncalibrated-nonstationary-anisotropic-autocorrelation-model>

1 **Ensemble Representation of Satellite Precipitation Uncertainty using an**
2 **Uncalibrated, Nonstationary, Anisotropic Autocorrelation Model**

3 **Samantha H. Hartke¹, Daniel B. Wright¹, Zhe Li², Viviana Maggioni³, Dalia B.**
4 **Kirschbaum⁴, Sana Khan^{4,5}**

5 ¹Department of Civil and Environmental Engineering, University of Wisconsin-Madison,
6 Madison, Wisconsin.

7 ²Department of Electrical and Computer Engineering, Colorado State University, Fort Collins,
8 Colorado

9 ³Department of Civil, Environmental, and Infrastructure Engineering, George Mason University.

10 ⁴NASA Goddard Space Flight Center, Greenbelt, MD, USA.

11 ⁵Earth System Science Interdisciplinary Center, University of Maryland, College Park, MD,
12 USA.

13 Corresponding author: Samantha Hartke (shartke@wisc.edu)

14 **Key Points:**

- 15 • High resolution precipitation ensemble fields are generated that represent the uncertainty
16 range of error-prone precipitation products.
- 17 • The space-time correlation structure of satellite precipitation error is modeled without
18 calibration and without ground-reference data.
- 19 • Precipitation ensembles demonstrate the ability to “bracket” ground-reference
20 observations at multiple space-time scales.
21

22 **Abstract**

23 The usefulness of satellite multi-sensor precipitation (SMP) and other satellite-informed
24 precipitation products in water resources modeling can be hindered by substantial errors which
25 vary considerably with spatiotemporal scale. One approach to cope with these errors is by
26 combining SMPs with ensemble generation methods, such that each ensemble member reflects
27 one plausible realization of the true—but unknown—precipitation. This requires replicating the
28 spatiotemporal autocorrelation structure of SMP errors. The climatology of this structure is
29 unknown for most locations due to a lack of ground reference observations, while the unique
30 anisotropy and nonstationarity within any particular precipitation system limit the relevance of this
31 climatology to the depiction of error in individual storm systems. Characterizing and simulating
32 this autocorrelation across spatiotemporal scales has thus been called a grand challenge within the
33 precipitation community. We introduce the Space-Time Rainfall Error and Autocorrelation Model
34 (STREAM), which combines anisotropic and nonstationary SMP spatiotemporal correlation
35 structures with a pixel-scale precipitation error model to stochastically generate ensemble
36 precipitation fields that resemble “ground truth” precipitation. We generate STREAM
37 precipitation ensembles at high resolution (1-hour, 0.1°) with minimal reliance on ground-
38 reference data, and evaluate these ensembles at multiple scales. STREAM ensembles consistently
39 “bracket” ground-truth observations and replicate the autocorrelation structure of ground-truth
40 precipitation fields. STREAM is compatible with pixel-scale error/uncertainty formulations
41 beyond those presented here, and could be applied globally to other precipitation sources such as
42 numerical weather predictions or “blended” products. In combination with recent work in SMP
43 uncertainty characterization, STREAM could be run without any ground data.

44 **1 Introduction**

45 Accurate, timely, high-resolution, and reliable precipitation data is critical for a range of
46 water modeling contents including floods, droughts, crop yields, and landslide hazards. Interest in
47 deploying such models at continental-to-global scales has grown in recent years. Examples include
48 the Famine Early Warning System (FEWS; Funk et al., 2019), the Global Land Data Assimilation
49 System (GLDAS; Rodell et al., 2004), the Global Flood Monitoring System (GFMS; Wu et al.,
50 2014), the Global Flood Awareness System (GloFAS; Alfieri et al., 2013), and the Landslide
51 Hazard Assessment for Situational Awareness (LHASA; Kirschbaum & Stanley, 2018). This
52 interest has been driven in part by increasing availability and accuracy of global precipitation
53 datasets to “fill in” where no ground-based sensors (e.g., rain gages or weather radar) exist. These
54 datasets include satellite multisensor precipitation (SMP) products, satellite-assimilating
55 numerical weather models, and “blended” options that combine the prior two, oftentimes with rain
56 gages (see Beck et al., 2017, Nogueira, 2020, and Sun et al., 2018 for recent reviews). While these
57 datasets share a common set of advantages—namely, global coverage at increasingly high
58 resolutions and ever lower latencies—and have improved in accuracy over time (Gebregiorgis et
59 al., 2018; Maggioni et al., 2016; Tang et al., 2020), they also share a general tendency towards
60 high systematic biases and random errors in both precipitation occurrence and rate (e.g., Nogueira,
61 2020; Tian & Peters-Lidard, 2010; Wright, 2018).

62 Errors in SMPs can arise from a variety of causes, including variable sensor accuracy and
63 sampling error from infrequent satellite overpasses, and are modulated by retrieval conditions
64 (e.g., Tan et al., 2016, 2018; Tian & Peters-Lidard, 2007). Validation studies have demonstrated
65 that errors tend to grow with latitude, precipitation intensity, terrain complexity, and in frozen or

66 mixed-phase precipitation conditions (e.g., Aghakouchak et al., 2011; Shige et al., 2013). Spatial
67 and temporal autocorrelation among SMP errors exists because the retrieval conditions and
68 sampling limits that impact a precipitation estimate at a given location and time tend to also impact
69 estimates that are nearby in space or time. This autocorrelation means that error properties vary
70 according to the level of spatial or temporal aggregation of the data (Quintero et al., 2016; Sarachi
71 et al., 2015; Tang et al., 2016); specifically, errors tend to diminish with increasing aggregation as
72 errors tend to cancel.

73 When used to force water prediction models, errors in precipitation products lead to errors
74 in model estimates of key variables such as streamflow, soil moisture, and groundwater storage
75 (e.g., Falck et al., 2015; Hossain et al., 2004; Maggioni et al., 2011; Schreiner-McGraw & Ajami,
76 2020; Serpetzoglou et al., 2010). Precipitation uncertainty and error also depend on spatial and
77 temporal resolution, with random errors tending to diminish with aggregation in space or time (P.
78 Kirstetter et al., 2018; Quintero et al., 2016; Sarachi et al., 2015). The same is true when erroneous
79 precipitation is used to predict streamflow, since river networks serve to aggregate rainfall-runoff
80 errors over spatial and temporal scales (Maggioni et al., 2013; Nikolopoulos et al., 2010). Because
81 of these issues and the limits they impose on large-scale water modeling, characterizing the space-
82 time autocorrelation structure of SMP error at arbitrary space-time scales has been called a “grand
83 challenge” for the precipitation community (Huffman et al., 2019). This work takes aim at this
84 grand challenge by attempting to model the space-time autocorrelation of SMP error; the proposed
85 approach could be applied to precipitation estimates from satellite-assimilating numerical weather
86 models or blended datasets due to the aforementioned broad similarities in their error/uncertainty
87 characteristics.

88 A significant challenge in addressing the space-time correlation structure of SMP error is
89 the nonstationarity and anisotropy of SMP error structures, which this study hypothesizes are
90 closely linked to the nonstationarity and anisotropy of rainfall fields themselves. For example, the
91 spatiotemporal structure of SMP error is likely very different during an elongated frontal storm
92 than during an isolated convective event or a highly-coherent tropical cyclone. This suggests that
93 it would likely prove very challenging to develop robust characterizations of these structures based
94 on a climatology of past storms, at least in a way that could be used operationally to supply
95 uncertainty information to end users. As will be seen, we avoid such an approach, diverging from
96 previous attempts to address this challenge.

97 It should be noted that the findings from the numerous validation studies that have assessed
98 SMP accuracy relative to ground-reference data (e.g., Asong et al., 2017; Gadelha et al., 2019; N.
99 Li et al., 2016; Tian et al., 2009 to name just a few) are not directly useful for SMP-based water
100 modeling applications. This is because the metrics they calculate—such as mean squared or
101 absolute errors, biases, and probabilities of detection and false alarms—do not readily translate
102 into “new” (i.e., better) precipitation fields that are needed as model inputs. They do, however,
103 highlight the challenge of providing better inputs by showing the prevalence, complexity, and
104 magnitudes of such errors. In recognition of this, Gebremichael et al. (2011) called for a shift in
105 SMP error characterization work towards “converting deterministic satellite rainfall estimates to
106 probabilistic form by overlaying an estimated error distribution around the deterministic rainfall
107 estimate.” In addition to our work presented here, several earlier efforts—detailed in Section 2—
108 have answered this call by introducing techniques that can generate distributions to characterize
109 the uncertainty of a specific SMP estimate.

110 While precipitation uncertainty is a random variable that can be described
111 probabilistically—typically via a probability distribution describing the possible “true” (but
112 unknown) precipitation rate at a given location and time—virtually all water prediction models are
113 formulated to ingest deterministic precipitation estimates. This disconnect between probabilistic
114 precipitation uncertainty and the need for deterministic input can be bridged by ensemble methods,
115 in which multiple realizations of possible precipitation can be generated which, in their totality,
116 reflect the range of uncertainty. These can be used to force an ensemble of water model simulations
117 that then hopefully provide useful estimates of hydrologic modeling uncertainty. Ensemble
118 methods are well-developed in the numerical weather prediction community, since members can
119 be created by perturbing the initial conditions, boundary conditions, or parameters of a numerical
120 atmospheric model (Cuo et al., 2011). Ensemble methods are much less developed in the SMP
121 community, for reasons that are difficult to summarize and beyond the scope of this work.
122 Nonetheless, a relatively limited set of studies have used ensemble approaches to assess
123 propagation of SMP error through hydrological and land surface models (Falck et al., 2015;
124 Gottschalck et al., 2005; Hossain & Anagnostou, 2005; Nijssen & Lettenmaier, 2004;
125 Serpetzoglou et al., 2010; Shrestha et al., 2020). These studies relied on ground reference data both
126 to characterize SMP uncertainty and to simulate the space-time correlation structure of SMP error.

127 This work introduces the Space-Time Rainfall Error and Autocorrelation Model
128 (STREAM), which combines the simulated nonstationary, anisotropic space-time autocorrelation
129 structure of precipitation error with pixel-scale estimates of precipitation uncertainty (Figure 1).
130 STREAM uses an ensemble-based approach, generating realizations of “reference-like”
131 precipitation fields—that is, fields that individually represent plausible realizations of the true
132 (unknown) precipitation based on satellite precipitation estimates, and together represent the range
133 of possible true rainfall (Figure 1). While not demonstrated here, the output from STREAM can
134 be ingested by hydrologic or land surface models without requiring any modification to these
135 models’ structures. Uniquely, STREAM’s space-time autocorrelation component is calibration-
136 free and requires no ground-reference data. This capability, demonstrated below, rests on the
137 hypothesis—which appears to be confirmed by our results—that the known space-time structure
138 of SMP fields themselves provides a useful approximation of the unknown space-time structure of
139 SMP error fields. This paper is organized as follows: Past error modeling work is summarized in
140 Section 2. Section 3 describes the study region and data. The methodologies for STREAM and a
141 previous error modeling approach, SREM2D, are covered in Section 4. Model results are shown
142 and discussed in Sections 5 and 6, respectively, and the contributions of this work are summarized
143 in Section 7.

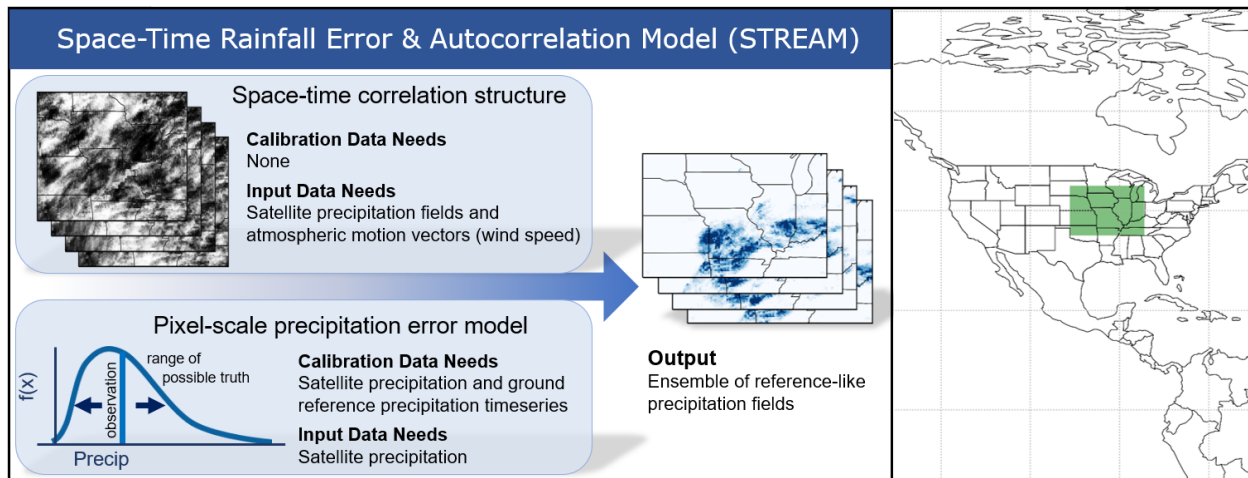


Figure 1. (left) Simple STREAM schematic and (right) study area highlighted in green in the central Continental United States (CONUS).

144

145 2 Background—Satellite Precipitation Error Modeling

146 Although the terms “error” and “uncertainty” are sometimes used interchangeably in the
 147 literature, in this paper we use error to refer to quantifiable differences between specific
 148 precipitation estimates and higher accuracy “ground truth” precipitation estimates, while using
 149 uncertainty to refer to the distribution of the possible true values relative to a precipitation estimate.
 150 For instance, the error for a given precipitation estimate is a deterministic value which can be
 151 calculated provided that high-quality ground truth data is available. In the absence of ground truth,
 152 this error is unknowable, and thus the best we can hope for is to know the uncertainty for that
 153 estimate—e.g. a range or distribution of plausible values which could be estimated through a
 154 variety of methods including those reviewed here. Regardless of our preferred terminology, the
 155 past literature uses the term “error model” to describe a method that provides an estimated
 156 distribution or range of possible true values based on an SMP observation. We keep with that
 157 terminological convention throughout this study.

158 Error models for SMP data can be placed in two categories: 1) pixel-scale error models,
 159 which characterize the SMP uncertainty associated with a single SMP estimate for a single control
 160 volume (invariably a grid cell) and time-step but do not consider the space-time autocorrelation
 161 structures between times and control volumes; and 2) space-time error models, which attempt to
 162 model the autocorrelation of SMP error. Both types, and the latter one in particular, have relied on
 163 extensive ground reference data for calibration. Additionally, space-time models have thus far
 164 neglected the nonstationarity and anisotropy in SMP error fields. Both categories face the
 165 challenge of representing the diversity of possible SMP errors—namely false alarms, missed
 166 precipitation, and hit errors (when a SMP estimate correctly detects rainfall but incorrectly
 167 estimates the magnitude). Some error models have focused entirely on hit cases while neglecting
 168 false alarms and missed cases (Reichle et al., 2007; Sarachi et al., 2015), while others handle
 169 rainfall detection and magnitude separately, resulting in either disjointed or overly complex model
 170 frameworks (Maggioni et al., 2014).

171 In pixel-scale error models, the uncertainty associated with a specific SMP estimate is
 172 described by a probability of precipitation and distribution of nonzero precipitation values which

173 are conditional on the value of a particular SMP observation. It is worthy to note that some pixel-
174 scale error models consider only hit cases and neglect the probability of precipitation component.
175 Pixel-scale error models in literature include the Censored Shifted Gamma Distribution (CSGD;
176 Wright et al., 2017), Precipitation Uncertainties for Satellite Hydrology (PUSH; Maggioni et al.,
177 2014), and Probabilistic QPE using InfraRed Satellite Observations (PIRSO; Kirstetter et al.,
178 2018), among others (Gebremichael et al., 2011). Sarachi et al. (2015) utilized a generalized
179 normal distribution to model SMP uncertainty across scales by interpolating pixel-scale model
180 parameters across various space-time resolutions. This approach considered hit cases only and
181 required calibration at several scales. Pixel scale error models are advantageous in that they are
182 trained using co-located timeseries of SMP and ground reference data and are therefore well suited
183 to calibration using available rainfall records from sparse rain gage networks. Pixel-scale error
184 models can also be “regionalized” by pooling together available training data from across a region
185 to calibrate a regional error model (Hartke et al., 2020; Khan & Maggioni, 2020; Li et al., 2021).
186 However, pixel-scale error models have no depiction of space-time autocorrelation; i.e. no way to
187 relate the uncertainty of an SMP estimate in one pixel to the uncertainty in nearby pixels in space
188 and time.

189 Space-time error models thus far have used calibration to characterize the climatological
190 autocorrelation structure of precipitation error. The Two-Dimensional Satellite Rainfall Error
191 Model (SREM2D) was developed by Hossain & Anagnostou (2006) in order to generate
192 ensembles of SMP-like rainfall fields which preserve the error characteristics of SMP fields.
193 Though SREM2D models the spatial correlation structure of SMP error fields as isotropic, these
194 error fields often exhibit substantial anisotropy, reflecting the anisotropy inherent in real storm
195 structures (Niemi et al., 2014; Zawadzki, 1973). Furthermore, SREM2D was not designed to
196 represent differences in spatial autocorrelation of SMP error across a study area (i.e., spatial
197 nonstationarity) and assumes that the average spatial correlation length calculated for a study
198 region is representative of that region for all locations and time steps. Since the spatial correlation
199 structure of SMP and SMP error can vary greatly at regional scales, this precludes SREM2D from
200 application to large (i.e. subcontinental-to-global) scales. Because SREM2D relies on a
201 climatological depiction of error autocorrelation, the model training and calibration process
202 requires a gridded (or at least spatially extensive) ground-based precipitation dataset. Such datasets
203 are lacking in many parts of the world (Kidd et al., 2017), further limiting is general applicability.
204 Though applied to radar rainfall rather than SMP, Villarini et al. (2009) introduced an error-driven
205 generator to stochastically perturb radar fields while accounting for the spatial correlation of
206 multiplicative error. However, that error model considered hit cases only, neglected temporal
207 correlation and anisotropy in error correlation structures, and used a computationally intensive
208 method to generate Gaussian noise (Villarini et al., 2009). Space-time error models that rely on
209 climatologically-calibrated parameters to simulate space-time correlation are not designed to
210 simulate the unique correlation structure – i.e. varying degrees of anisotropy and correlation
211 distances in space and time – of precipitation error that is associated with each new storm system.

212 The STREAM framework introduced in this article utilizes a calibration-free approach to
213 modeling the space-time autocorrelation structure of precipitation error and provides a way to
214 leverage pixel-scale estimates of precipitation uncertainty in space and time. Although this work
215 utilizes a subcontinental study area, STREAM’s approach of reproducing the local spatial
216 autocorrelation structures of SMP fields enables continental- to global-scale application.

217 **3 Study Region and Data**

218 3.1 Study Region

219 The study area covers the central U.S. (Figure 1; 100° to 85° W, 35° to 45° N), a region
220 known for high agricultural production (Prince et al., 2001) and also marked by flood events often
221 caused by heavy, long-lasting precipitation that severely impact local communities (e.g. the 1993
222 Mississippi River and 2008 Iowa flood events; Budikova et al., 2010; Najibi et al., 2016; Nakamura
223 et al., 2013; Smith et al., 2013). Intense events provide a significant portion of the region's annual
224 precipitation total, and convective storm systems are frequent during the warm summer period.
225 The topography of this region is fairly uniform (Andresen et al., 2012).

226 3.2 Rainfall Data

227 The NASA Integrated MultisatellitE Retrievals for Global Precipitation Measurement
228 (IMERG) Version 06 product is available globally at a 30-minute, 0.1° resolution and consists of
229 three latency options (Huffman et al., 2019): IMERG Early (4-hour latency; lacks some data
230 sources and data processing elements of longer latencies), IMERG Late (12-hour latency), and
231 IMERG Final product (approximately 2.5-month latency; includes a gage-based correction).
232 IMERG precipitation estimates are calculated by merging data from passive microwave (PMW)
233 sensors, intercalibrating PMW estimates with a dual-frequency precipitation radar aboard the
234 Global Precipitation Measurement (GPM) Core Observatory satellite, and interpolating (or
235 “morphing”) the resulting estimates in time using water vapor motion vectors from MERRA-2 and
236 GEOS-5 (see Huffman et al., 2019; Tan et al., 2016 for more details). This study uses IMERG
237 Early, aggregated to the hourly scale to match the radar-gage ground reference product; the
238 approach could be readily applied to other IMERG latencies, as well as to other SMP products.

239 The NEXRAD Stage IV radar-gage product, available over CONUS at an hourly, roughly
240 1/24° resolution (Lin, 2011), is used as the ground reference in this study. Although NEXRAD's
241 Stage IV product contains errors stemming from issues such as beam blockage and range from the
242 nearest radar, we assume that the errors in this product are infrequent and negligible relative to
243 IMERG, consistent with previous SMP studies (e.g. Aghakouchak et al., 2011) and consistent with
244 our own prior experience using the dataset in this region. We upscaled Stage IV to IMERG's native
245 0.1° resolution using bilinear interpolation.

246 IMERG-Early (hereinafter IMERG) and Stage IV data from 2005-2007 were used for
247 calibration of all models, while data from 2008-2013 for validation. To minimize issues related to
248 frozen precipitation and maintain an accurate ground-reference during model calibration and
249 validation, Stage IV and IMERG data were used only for March through October, excluding
250 months with greater likelihood of frozen precipitation in the study area (November-February). This
251 is admittedly a limitation of our study that should be addressed in the future. For both Stage IV
252 and IMERG, the threshold for precipitation detection was set to 0.1 mm/hr, below which all hourly
253 estimates were set to zero. This detection threshold is consistent with previous SMP studies
254 (Germann & Zawadzki, 2002; Li et al., 2021).

255 3.3 Wind Data

256 As an approximation of the “steering winds” that govern the motion of storm systems, 850
257 mb wind fields were retrieved from the global MERRA-2 reanalysis product (Gelaro et al., 2017)
258 at a hourly 0.5° by 0.625° resolution. These were regridded to 0.1°. These wind fields were used

259 together with IMERG fields to simulate the temporal evolution and autocorrelation structure of
 260 SMP error in STREAM (described in Section 4.2). Other sources of motion vectors could be used,
 261 including potentially those used in IMERG's aforementioned "morphing" space-time interpolation
 262 scheme. Those motion vectors are not publically available, however, so were not considered here.
 263 This point is discussed further in Section 6.4.

264 4 Methods

265 4.1 Censored Shifted Gamma Distribution Error Model

266 The Censored Shifted Gamma Distribution Error (CSGD) model framework was
 267 introduced by Scheuerer and Hamill (2015) to model uncertainty in numerical weather forecasts,
 268 and was adapted in Wright et al. (2017) to characterize pixel-scale SMP error across CONUS. The
 269 CSGD is an adaptation of the two-parameter gamma distribution (here written in terms of its mean
 270 and standard deviation, but which can be reparametrized in terms of shape and scale parameters)
 271 with an additional "shift" parameter δ that shifts the probability density function (PDF) leftward
 272 (Figure 2a). The density left of zero represents the probability of zero precipitation, while the
 273 density at any value greater than zero represents the likelihood of that amount of precipitation
 274 (Figure 2a, 2b). The shifted distribution is then left-censored at zero, replacing all negative values
 275 with zero. While previous precipitation error models either focused only on hit errors or required
 276 separate components to model rainfall occurrence and magnitude (see Section 2), the CSGD error
 277 model characterizes both the discrete and continuous components of satellite precipitation error
 278 using this single distribution. A regression model is trained based on contemporaneous co-located
 279 SMP and ground-truth observations to produce model parameters $\alpha_1, \alpha_2, \alpha_3, \alpha_4, \dots$ and, at any time
 280 t , unique "conditional" CSGD parameters $\mu(t), \sigma(t)$, and $\delta(t)$ as a function of those parameters and
 281 the SMP estimate $R_s(t)$:

$$282 \quad \mu(t) = \frac{\mu_c}{\alpha_1} \log_{1p} \left\{ \text{expm1}(\alpha_1) \left[\alpha_2 + \alpha_3 \frac{R_s(t)}{\bar{R}} \right] \right\} \quad \text{Eq. 1}$$

$$283 \quad \sigma(t) = \alpha_4 \sigma_c \sqrt{\frac{\mu(t)}{\mu_c}} \quad \text{Eq. 2}$$

$$284 \quad \delta(t) = \delta_c \quad \text{Eq. 3}$$

285 where \bar{R} is the mean of the SMP timeseries during the training period and $(\mu_c, \sigma_c, \delta_c)$ are the
 286 parameters of the climatological CSGD, a CSGD fit to the SMP time series. The regression model
 287 defined by Equations 1-3 allows the model to capture nonlinear behavior of SMP error across
 288 increasing precipitation rates. A simpler linear regression system can also be used in the CSGD
 289 error model framework by altering Eq. 1 (not shown; Scheuerer et al., 2015; Wright et al., 2017).
 290 The regression framework can also incorporate additional contemporaneous covariates $C_1(t)$,
 291 $C_2(t), \dots, C_n(t)$, such as temperature or precipitable water, that could help to further characterize
 292 SMP uncertainty. These covariates are incorporated into the regression framework using an
 293 adjusted version of Eq. 1:

$$294 \quad \mu(t) = \frac{\mu_c}{\alpha_1} \log_{1p} \left\{ \text{expm1}(\alpha_1) \left[\alpha_2 + \alpha_3 \frac{R_s(t)}{\bar{R}} + \alpha_5 \frac{C_1(t)}{c_1} + \alpha_6 \frac{C_2(t)}{c_2} + \dots \right] \right\} \quad \text{Eq. 4}$$

295 For more information on the CSGD error model framework, see Scheuerer and Hamill
 296 (2015) and Wright et al. (2017).

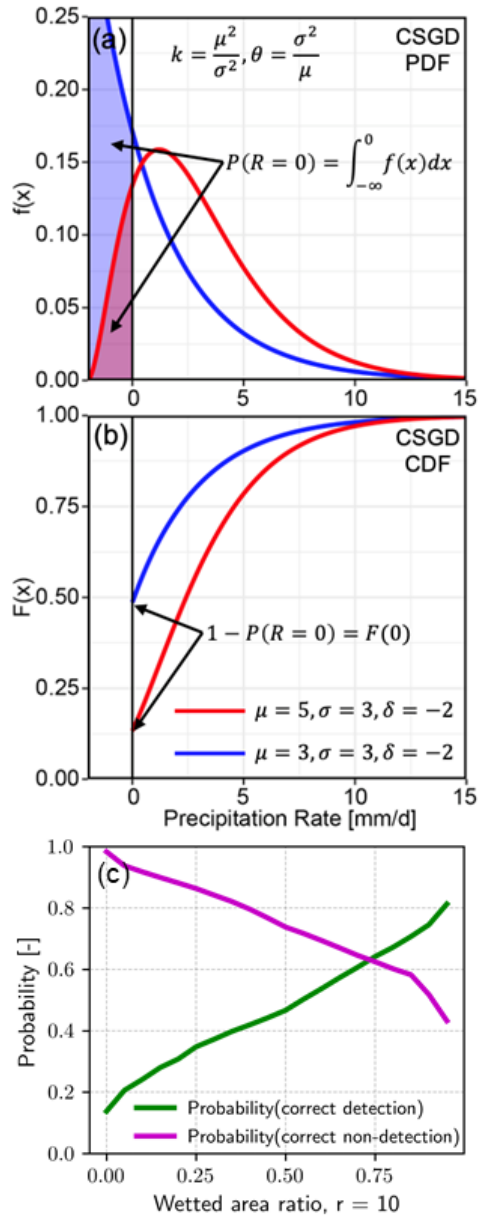


Figure 2. (a) Probability density function (PDF) and (b) cumulative density function (CDF) of two hypothetical censored shifted gamma distributions (CSGDs). (c) Observed probability of IMERG correct detection of nonzero rainfall (green) and probability of IMERG correct non-detection of rainfall (purple) as a function of the wetted area ratio (WAR) covariate. (c) uses data from entire study area for the period 2005-2007.

In this study, we use wetted area ratio (WAR) for the first time as a covariate in the CSGD error model. WAR for any IMERG estimate $R_s(t)$ at a given pixel is the proportion of pixels within a distance of r pixels that record nonzero rainfall at time t . WAR ranges from a value of 0 when no pixels within radius r have a nonzero precipitation rate, to 1, when all pixels within radius r have precipitation. Because WAR captures the spatial “context” of an IMERG observation, it is a useful covariate for predicting detection/non-detection performance within the CSGD framework. Figure 2c demonstrates that the probability of an IMERG estimate of nonzero rainfall being a correct detection is much greater if the associated WAR is high (i.e. close to 1.0) than if it is low. Likewise, the probability of IMERG correctly not detecting rainfall is highest when WAR is close to 0 (Figure 2c). A radius of $r = 10$ pixels was used to calculate WAR in this work; higher and lower values of r did not significantly alter CSGD error model performance (results not shown).

In this study, CSGD error model parameters are trained using timeseries “pooled” together from 25 co-located IMERG and Stage IV pixels (i.e. a $0.5^\circ \times 0.5^\circ$ area). CSGD error model training for each $0.5^\circ \times 0.5^\circ$ window in the study area is performed using the regression system defined in Equations 1-3 with the WAR covariate. The parameter estimation is completed via mean continuous ranked probability score (CRPS) minimization methods described in Scheuerer et al. (2015). Using timeseries from multiple pixels reduces sampling error and generates a more robust error model than model training using timeseries from a single IMERG pixel (not shown). This approach is suitable for the relatively homogenous terrain in the study area but may not be appropriate in more complex terrain where IMERG error characteristics are more closely tied to terrain heterogeneity.

336 4.2 The Space-Time Rainfall Error and Autocorrelation Model (STREAM)

337 4.2.1 Nonstationary anisotropic stochastic noise from pySTEPS

338 Nerini et al. (2017) introduced a non-stationary stochastic generator for radar precipitation
 339 fields using the short-space Fourier transform (SSFT). The Fourier power spectrum of a
 340 precipitation field (e.g. from weather radar or SMP) is convolved with Gaussian white noise to
 341 generate correlated Gaussian noise fields and ultimately produce an ensemble of precipitation
 342 forecasts which maintain the anisotropy and spatial correlation structure of observed radar rainfall
 343 fields. This methodology reproduces both the global and local power spectra of radar fields by
 344 using a moving window scheme. This moving window can thus capture spatial nonstationarity in
 345 field properties, since at any particular location the correlated noise is based on properties within
 346 the window. This SSFT-based non-stationary noise generator has since been incorporated into the
 347 pySTEPS Python library for short-range probabilistic precipitation forecasting, as a tool for
 348 generating ensemble nowcasts (Pulkkinen et al., 2019). While Nerini et al. (2019) used this tool to
 349 generate stochastic precipitation fields that replicate the local spatial correlation structure of
 350 observed radar rainfall fields, the authors emphasized that it could be applied to other applications
 351 involving complex non-stationary fields. Notably, this approach requires no calibration against
 352 ground truth measurements or parameterization of long-term precipitation behavior.

353 4.2.2 Correlated noise ensemble generation

354 In the first step of STREAM, the pysteps noise generator described in Section 4.2.1 is
 355 applied to stochastically generate Gaussian noise that replicates the local spatial correlation
 356 structure of an IMERG field, including anisotropy (Figure 3). After the initial noise field has been
 357 created for each ensemble member, each noise field is advected at an hourly time step via steering
 358 winds (described in Section 3.3) using a semi-Lagrangian scheme. In such a scheme, a time
 359 derivative (in this application, 850 mb wind vectors) is used to calculate where the value arriving
 360 at a grid cell, termed the arrival point, originated from in the previous time step (Lauritzen et al.,
 361 2011; Staniforth & Cote, 1991). This semi-Lagrangian scheme is advantageous over a strictly
 362 Lagrangian one because it does not allow individual parcels (in our case, noise values) to all advect
 363 into a single region and leave some regions without parcels. Our semi-Lagrangian scheme also
 364 incorporates a new instance of correlated noise, or a “shock term” (Nerini et al., 2017) which is
 365 the second term on the righthand side of Equation 5:

$$366 \quad n_{t,i,j} = \alpha n_{t-1,i-v_t,j-u_t} + \sqrt{1 - \alpha^2} \tilde{n}_{t,i,j} \quad \text{Eq. 5,}$$

367 where $n_{t,i,j}$ is a noise value to be calculated at time t and position (i, j) in the field and $n_{t-1,i-v_t,j-u_t}$
 368 is the noise value that has been advected by north-south and east-west wind vectors v_t and u_t from
 369 position $(i - v_t, j - u_t)$ at time step $t - 1$ to position (i, j) at time step t . v_t and u_t are obtained by
 370 multiplying MERRA2 wind vectors, originally in units of m/s , by 3600 seconds and dividing by
 371 11,000 m, the approximate width of an IMERG pixel, to obtain units of $0.1^\circ \text{ pixel } hr^{-1}$. \tilde{n}_t is a new
 372 correlated Gaussian noise field based on the structure of IMERG at time t . The shock term is used
 373 to perturb the noise field and to incorporate the current IMERG spatial correlation structure, \tilde{n}_t ,
 374 into the noise field at each time step. This allows the noise field to evolve over time and to reflect
 375 the nonstationary spatial correlation structure of IMERG and IMERG error. We assume that the
 376 error fields are first order autoregressive in time, calculating α as the Pearson correlation
 377 coefficient between IMERG fields at time t and $t - 1$ (Figure 3). Analysis of the temporal

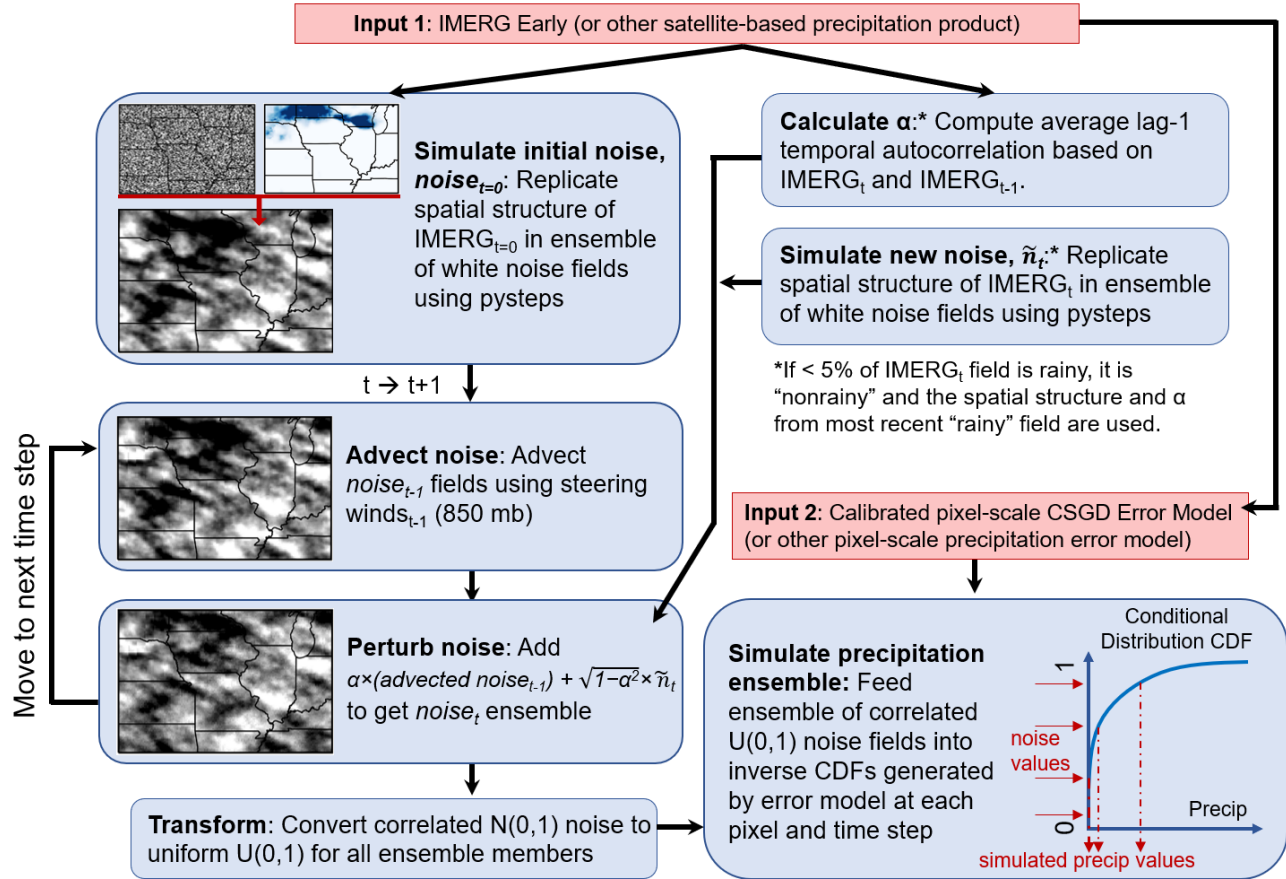


Figure 3. Schematic of STREAM methodology

378 autocorrelation function of IMERG error fields supports this autoregressive assumption (results
 379 not shown). After the noise ensemble has been generated for all time steps in the study period, the
 380 correlated Gaussian noise ensemble $N(0,1)$ is transformed to uniform noise $U(0,1)$ using the error
 381 function:

$$382 \quad n_{uniform} = 0.5 \left[1 + \operatorname{erf} \left(\frac{n_{gaussian}}{\sqrt{2}} \right) \right] \quad \text{Eq. 6.}$$

383 where $n_{gaussian}$ is the noise field described in Equation 5.

384 Note that correlated noise fields rn_t and temporal coefficient α are only calculated based on
 385 IMERG at time t when the IMERG field is “rainy,” defined as when at least 5% of the study area
 386 registers rainfall (Figure 3). During time steps with non-rainy fields, which are frequent at the
 387 hourly scale, the spatial correlation structure from the most recent rainy field is used to generate
 388 rn_t . In either case, no parameters depend on a long-term climatology.

389 4.2.3 Precipitation ensemble generation

390 In the final step of STREAM, the correlated uniformly-distributed noise ensemble is
 391 combined with the CSGD error model. The CSGD model and training scheme methodology were
 392 briefly described in Section 4.1. The standard uniform noise values from the semi-Lagrangian
 393 scheme (Section 4.2.2) are inputted to the inverse CDF of the conditional CSGD generated at each
 394 time step and pixel. Thus, each noise value corresponds to a value of possible true precipitation

395 conditional on a given IMERG estimate and associated WAR (Section 4.1), correlated with
 396 surrounding pixels. The uniform noise ensemble is censored at 0.995 to guard against
 397 unrealistically extreme precipitation values generated when very high noise values are used to
 398 select a precipitation value from conditional CSGDs with long tails. The output of STREAM
 399 consists of an ensemble of three-dimensional (north-south, east-west, time) precipitation fields,
 400 with each ensemble member representing one realization of the possible true precipitation across
 401 the study region for all time steps in the study period.

402 We also generated “uncorrelated” precipitation ensembles by using white (uncorrelated)
 403 noise as input to the inverse CDF of conditional CSGDs, thus neglecting spatial and temporal
 404 correlation of errors. The precipitation ensemble generated in this way is henceforth referred to as
 405 the uncorrelated ensemble, though they are not strictly uncorrelated since the resulting
 406 precipitation fields will inevitably exhibit some autocorrelation stemming from the IMERG
 407 precipitation rates (albeit much weaker than that of the ground-reference, IMERG, or
 408 autocorrelated noise fields).

409 4.3 SREM2D

410 The SREM2D error model was designed to generate ensembles of “satellite-like” fields
 411 that replicate the error properties of an SMP dataset relative to a ground-reference (Hossain et al.,
 412 2006). SREM2D separately accounts for the spatial correlation of detection errors and precipitation
 413 rate errors, and uses the Turning Bands algorithm (Mantoglou & Wilson, 1982) to generate 2-D
 414 Gaussian noise with correlation lengths matching that of the conditional error of SMP fields. In
 415 this work, SREM2D is run “in reverse” to generate reference-like rainfall fields that are closer to
 416 the ground-reference by replicating the error properties of Stage IV relative to IMERG Early.
 417 SREM2D has been used in this fashion previously in Falck et al. (2015) and Maggioni et al. (2013)
 418 to improve model-simulated streamflow estimates compared against hydrographs from SMPs.
 419 SREM2D parameters are trained using Stage IV and IMERG data for the 2005-2007 training
 420 period detailed in Section 3.2 and are listed in Table S1. Consistent with earlier SREM2D studies,
 421 additional trial-and-error calibration is needed (specifically, adjustment of the mean parameter) to
 422 minimize bias in SREM2D-perturbed fields. Note that these error parameters are calculated for the
 423 reference, Stage IV, relative to IMERG, highlighting SREM2D’s need for ground reference data
 424 to characterize not only pixel-scale errors (akin to the CSGD approach) but also the spatiotemporal
 425 autocorrelation process (unlike STREAM, which doesn’t require ground reference for this
 426 purpose).

427 4.4 Ensemble performance metrics

428 STREAM, SREM2D, and the uncorrelated ensembles were run at an hourly time step with
 429 an ensemble size of 50 for the evaluation period 2008-2013, excluding winter months (November–
 430 February). The spatial autocorrelation function (ACF), temporal ACF, probability of detection
 431 (POD), probability of false alarm (POFA), root mean square error (RMSE), and Containing Ratio
 432 were used to evaluate the performance of IMERG, the STREAM ensemble, the uncorrelated
 433 ensemble, and the SREM2D ensemble. The Containing Ratio (CR) is the proportion of observed
 434 data bracketed by the range of an ensemble, and has been used within the forecast verification and
 435 runoff modeling community to assess ensemble accuracy (Franz & Hogue, 2011; Xiong &
 436 O’Connor, 2008).

$$437 \quad CR = \frac{1}{n} \sum_{t=1}^n I[R_{obs}(t)] \quad \text{Eq. 7.}$$

438 where $I[\cdot]$ is an indicator function that equals 1 when the observed rainfall $R_{obs}(t)$ falls between
439 the lowest and highest values of the ensemble at time t and that equals 0 when the observation falls
440 outside ensemble bounds. For deterministic evaluation metrics, including RMSE, POD, and
441 POFA, the mean of the ensemble was evaluated.

442 Spatial and temporal linear autocorrelation functions were calculated for each ensemble
443 member to assess the ability of STREAM to generate reference-like precipitation fields in space
444 and time. We note that assessing the space-time correlation structure of precipitation ensemble
445 fields is not equivalent to assessing the space-time correlation structure of the SMP error
446 introduced to create these fields; however, the correlation structures of SMP error fields can vary
447 depending on the specific mathematical definition of SMP error. Since precipitation fields that
448 resemble a ground-reference are the ultimate objective of an ensemble-based SMP error model,
449 we chose to evaluate the ability of STREAM ensemble members to replicate the space-time
450 correlation structures of Stage IV.

451 The above metrics were calculated for all precipitation datasets and ensembles at four
452 space-time resolutions: 1-hour 0.1° , 1-hour 0.25° , 24-hour 0.1° , and 24-hour, 0.25° . Precipitation
453 fields were regridded to coarser spatial resolutions using bilinear interpolation.

454 **5 Results**

455 Figure 4 shows IMERG, Stage IV, and outputs from the uncorrelated ensemble, STREAM
456 autocorrelated noise and ensemble, and SREM2D ensemble for a six-hour period during a storm
457 event in 2008 that led to heavy flooding in Cedar Rapids and Iowa City. Ensemble members shown
458 in Figure 4 were chosen at random. While the uncorrelated ensemble fields do not resemble
459 precipitation structures observed by Stage IV, STREAM and SREM2D fields visually resemble
460 realistic precipitation structures from Stage IV, and STREAM also reproduces the observed
461 anisotropy. The spatial correlation features generated in the STREAM noise fields clearly translate
462 to similar spatial correlation features in STREAM precipitation fields. SREM2D fields exhibit less
463 fine-scale anisotropic detail than STREAM, presumably due to its isotropic formulation.

464 Figure 5 provides additional event-scale analysis of STREAM, showing cumulative hourly
465 precipitation and daily precipitation rates for a heavy rainfall event in June 2013 in southcentral
466 Wisconsin. Area-averaged precipitation was calculated for the inset area in Figure 5a. The spatial
467 autocorrelation function of precipitation within the inset area was also calculated to assess
468 STREAM ensemble performance during this event, confirming STREAM ensemble members'
469 ability to replicate the spatial structure of Stage IV rainfall (Figure 5c). The STREAM ensemble

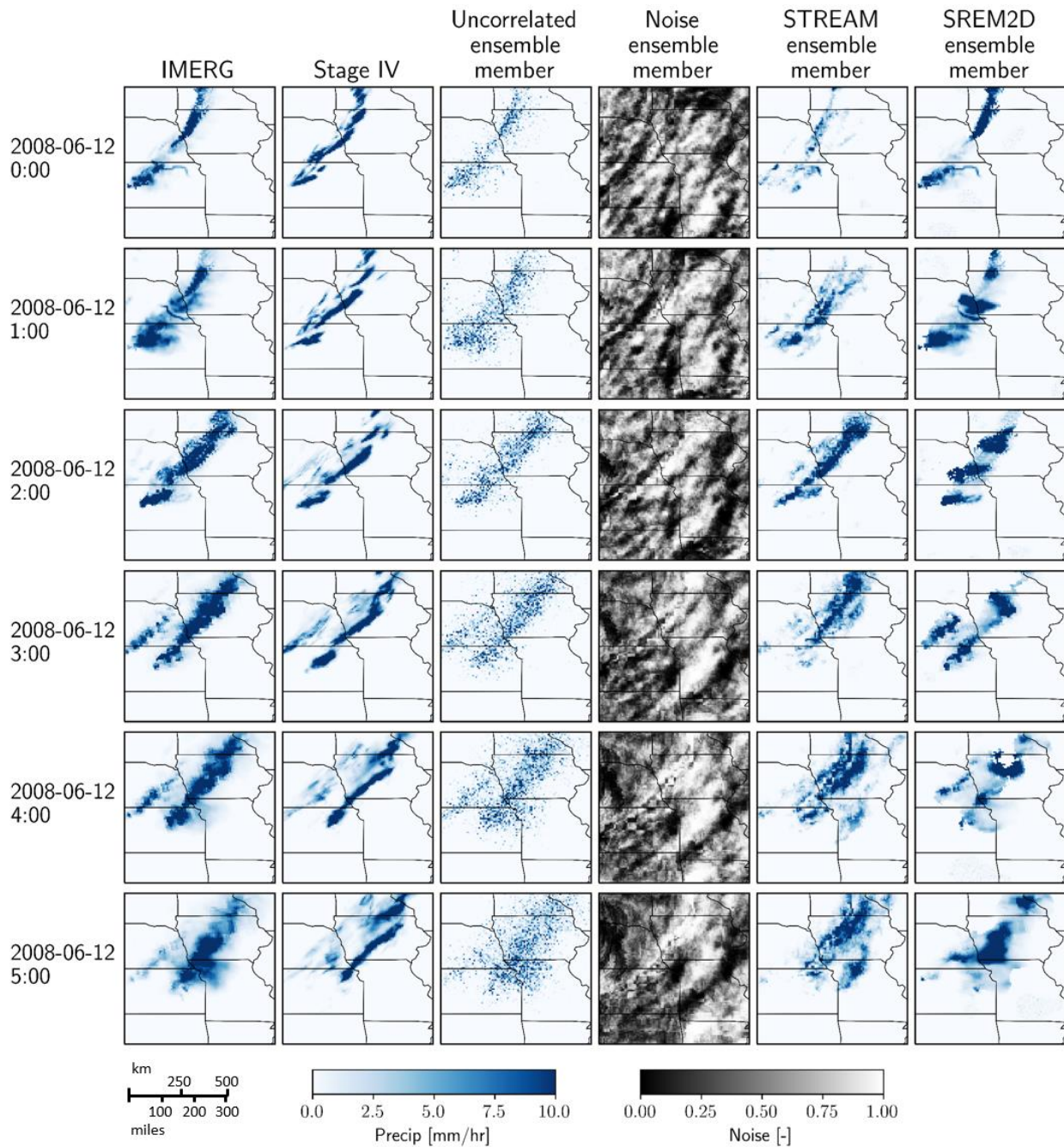


Figure 4. Example output of STREAM and other error modeling approaches. From left column to right column: IMERG, Stage IV, uncorrelated ensemble member, correlated noise ensemble member generated by STREAM, STREAM precipitation ensemble member, and SREM2D ensemble member during heavy rainfall event in study area on June 12, 2008. Ensemble members were chosen at random.

470 brackets the observed cumulative precipitation over the course of the event, reducing IMERG's
 471 stark overestimation (Figure 5b), and generally brackets observed precipitation rates at the daily
 472 scale, with the exception of two days (Figure 5d). Note that the uncertainty described by the range
 473 of the STREAM ensemble is small on days with low IMERG estimates, but widens when IMERG

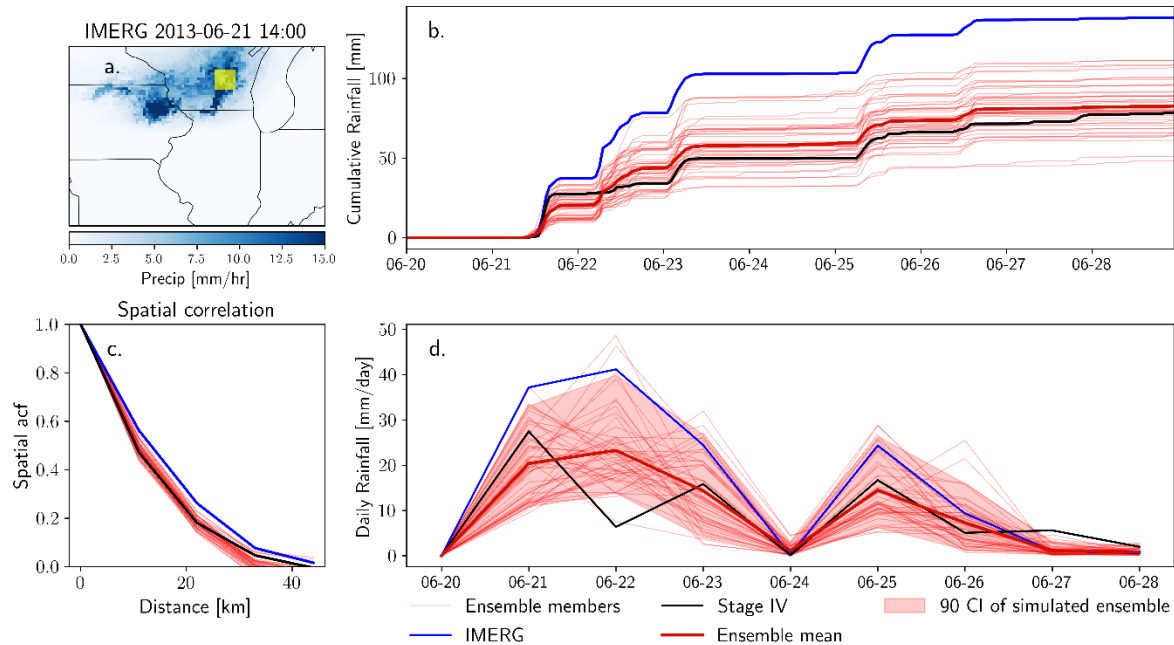


Figure 5. STREAM ensemble performance during 2013 flooding event in southcentral Wisconsin. (a) Area average precipitation is calculated over inset area in southcentral Wisconsin, denoted by yellow box (b) Hourly cumulative precipitation over course of event (c) Spatial autocorrelation function (ACF) calculated for precipitation in inset area over course of event (d) Daily precipitation rate over course of event.

474 observes nonzero rainfall, reflecting the greater range of random error in nonzero IMERG
 475 estimates (Figure 5d).

476 Figure 6 presents a seasonal-scale analysis of STREAM results, showing cumulative area-
 477 averaged spring precipitation (March–May) over eastern Iowa for all years in the validation period.
 478 The ensemble spread brackets the cumulative precipitation at the end of May in all years,
 479 regardless of whether IMERG over- or underestimates spring cumulative precipitation, except
 480 2008, a year in which IMERG significantly underestimated cumulative precipitation. Precipitation
 481 in 2008 was well above the climatological average for all months shown in Figure 6, due in part
 482 to unprecedented rainfall occurring in the end of May and early June —conditions that likely pose
 483 a particular challenge for error modeling.

484 Figure 7 presents RMSE, POD, and POFA calculated over the entire study area and
 485 validation period for IMERG and all ensemble products at four space-time resolutions. The RMSE
 486 of IMERG and all ensemble means increases sharply for extreme hourly rainfall rates (> 8 mm/hr).
 487 The STREAM ensemble mean and uncorrelated ensemble mean exhibit reduced RMSE at all
 488 scales and across all rain rates, with the exception of heavy rain rates at an hourly scale. The
 489 SREM2D ensemble mean has a very similar RMSE to IMERG at all scales. The higher RMSE of
 490 the SREM2D ensemble mean relative to the STREAM ensemble aligns with results from Maggioni
 491 et al. (2011), who found that the relative RMSE of SREM2D-perturbed rainfall was slightly greater
 492 than that of the original satellite product.

493 The STREAM ensemble mean and uncorrelated ensemble mean exhibit higher POD across
 494 all space-time scales. Notably, the STREAM ensemble mean and uncorrelated ensemble mean are

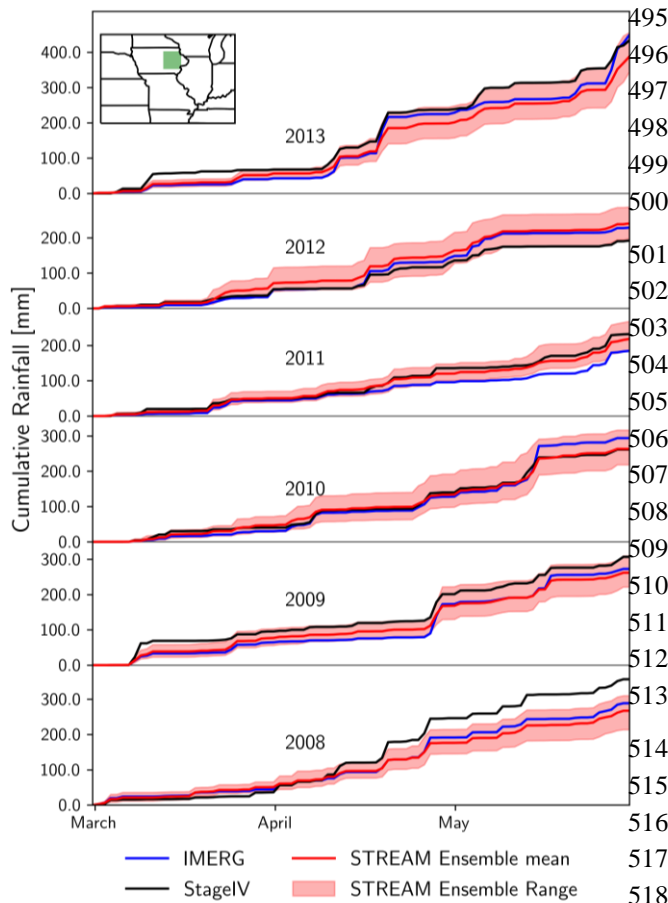


Figure 6. Cumulative area average rainfall over eastern Iowa subregion (green box in upper left inset map) estimated by IMERG (blue), Stage IV (black) and the STREAM ensemble (red).

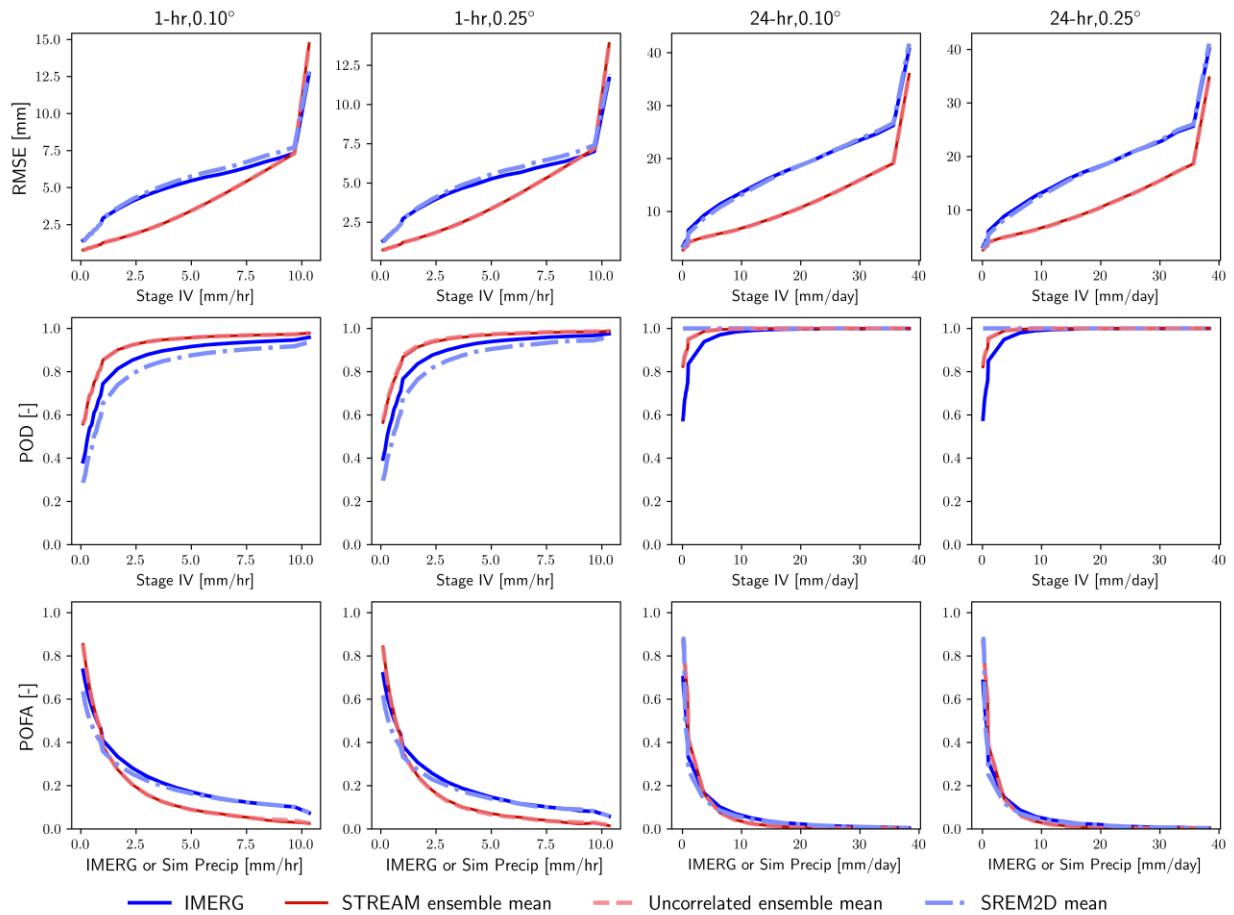
able to simultaneously increase the POD while reducing the POFA at the hourly scale for precipitation rates greater than 1 mm/hr. The POFA of the STREAM and uncorrelated ensemble means are slightly higher than IMERG at the daily scale.

The spatial autocorrelation functions in the x - and y -directions (east-west and north-south, respectively) and the temporal autocorrelation function of IMERG, Stage IV, and ensemble fields are shown in Figure 8. Only ten members of each ensemble from STREAM, SREM2D, and the uncorrelated ensemble are displayed for clarity; since the ACFs are calculated over a long validation period, the ACFs of individual members within each error modeling method are nearly identical.

The correlation structure of STREAM ensemble fields nearly matches that of Stage IV at every scale (Figure 8), although the spatial ACF of ensemble fields—both in the x - and y -directions—is slightly lower than the spatial ACF of Stage IV. The uncorrelated ensemble members exhibit much lower spatial and temporal autocorrelation than Stage IV at the hourly scale, with the greatest difference at the finest spatial resolution.

Once ensemble fields are aggregated to a coarser resolution (24-hr, 0.25°), all error model ensembles roughly replicate the average spatial and temporal autocorrelation functions of Stage IV. SREM2D ensemble members exhibit lower temporal autocorrelation than Stage IV at the hourly scale.

The Containing Ratios (CR) of the STREAM ensemble, SREM2D ensemble, and uncorrelated ensemble as a function of precipitation rate across four resolutions are presented in Figure 9. The STREAM ensemble consistently maintains a high CR (generally >0.8) across scales, though it dips at extreme rain rates. The STREAM ensemble brackets approximately 50% (70%) of the instances when ground-reference rainfall is greater than 8 mm/hr (35 mm/day) at an hourly (daily) resolution. SREM2D has a high containing ratio for Stage IV observations of zero precipitation but experiences a sharp decrease for nonzero values. The SREM2D ensemble fails to capture many of the nonzero ground-reference observations that the STREAM ensemble and uncorrelated ensemble successfully bracket. The performance of the uncorrelated ensemble degrades with increasing scale; at a daily, 0.25° scale, the uncorrelated ensemble fails to capture over 60% of the instances when the ground-reference observes rain rates greater than 30 mm/day.



540

541 **Figure 7.** RMSE (top row), probability of detection (POD; middle row), and probability of false
 542 alarm (bottom row) for IMERG (blue), mean of STREAM ensemble (red), mean of uncorrelated
 543 ensemble (dashed pink), and mean of SREM2D ensemble (light blue) across four space-time
 544 resolutions. Metrics are calculated using study area-wide data for 2008-2013. STREAM ensemble
 545 and uncorrelated ensemble means are essentially identical (and are therefore difficult to distinguish
 546 from one another in the above plots).

547

548

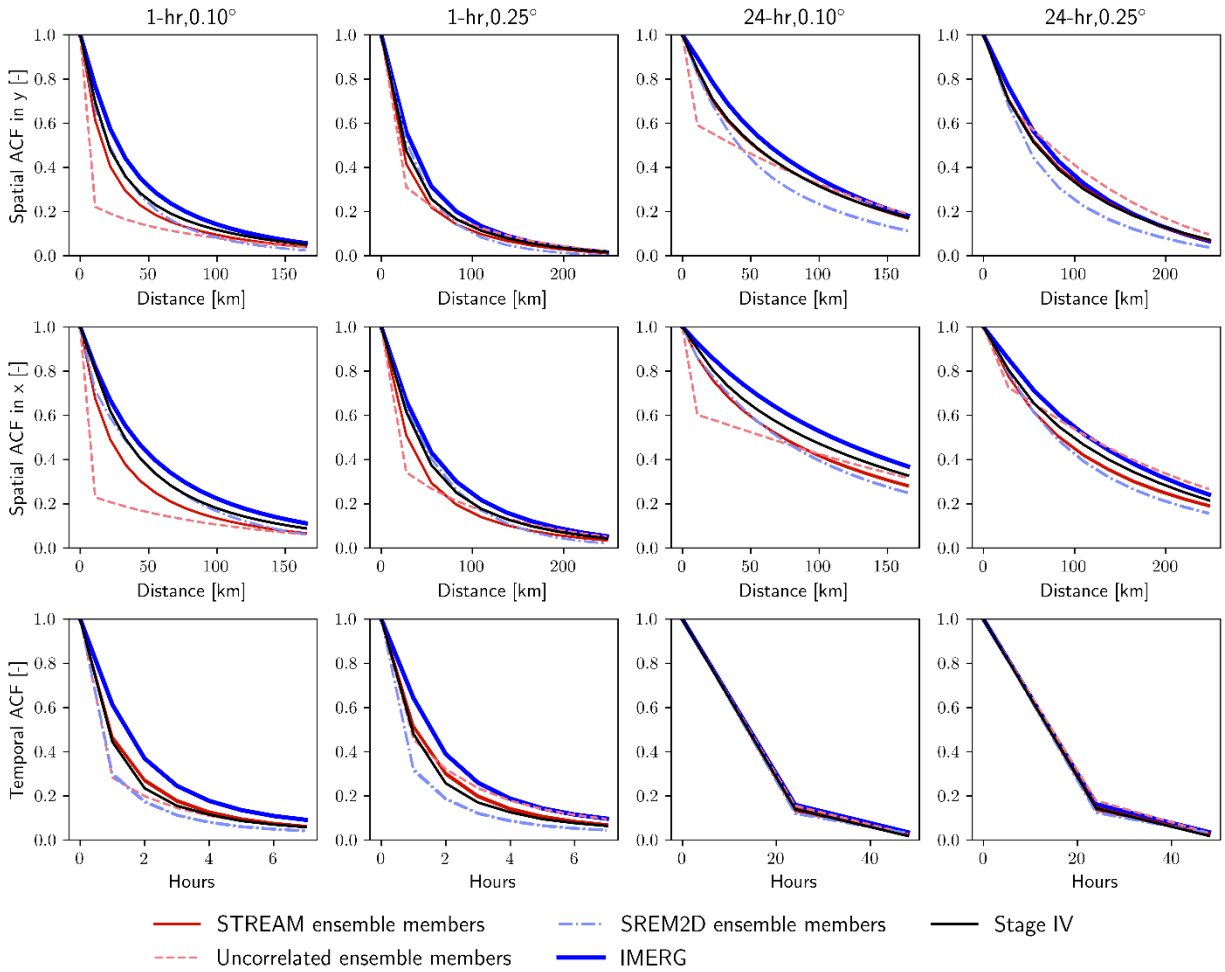
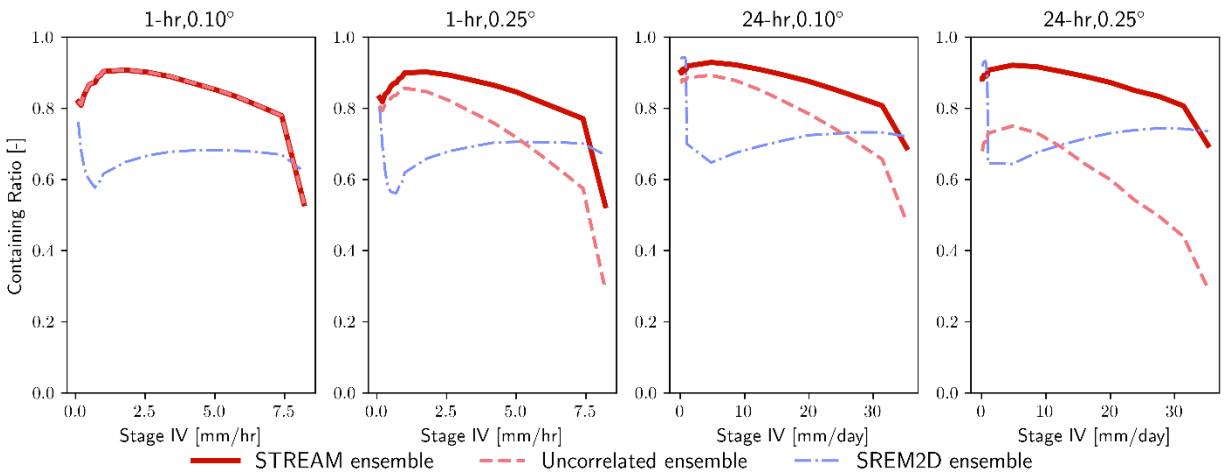


Figure 8. (Top) Spatial autocorrelation function (ACF) in the y-direction, (Middle) Spatial ACF in the x-direction, and (Bottom) Temporal ACF calculated for IMERG, Stage IV and 10 simulated rainfall ensemble members each from STREAM, SREM2D, and the uncorrelated ensemble at four resolutions.



549 **Figure 9.** Containing ratio (CR) of simulated ensembles at four resolutions.

550 6 Discussion

551 6.1 Performance of STREAM across multiple spatio-temporal scales

552 While the full STREAM ensemble at any given point in time and space represents the range
553 of random error associated with IMERG, the ensemble mean represents the IMERG estimate
554 adjusted only for systematic bias. Therefore, the mean of the ensemble will outperform individual
555 ensemble members in terms of RMSE by strictly addressing systematic bias, but cannot capture
556 the range of IMERG uncertainty on its own. The mean of the STREAM ensemble consistently
557 reduces RMSE relative to IMERG across scales and rain rates except for hourly intensities greater
558 than 10 mm/hr (Figure 7). This is likely due to the difficulty of predicting missed cases associated
559 with heavy ground-reference rainfall. The STREAM ensemble mean has a higher or similar
560 probability of detection relative to IMERG across rain rates and scales, with the greatest
561 improvements achieved at lower precipitation rates (Figure 7). A portion of this improvement is
562 due to the incorporation of the wetted area ratio (WAR) in the pixel-scale CSGD error model,
563 which helps predict IMERG missed cases based on the presence or absence of nearby IMERG
564 rainfall (Supplemental Figure S1). The probability of false alarm is slightly higher for the
565 STREAM ensemble mean relative to IMERG at rates below 1 mm/hr at the hourly scale and below
566 10 mm/day at the daily scale. At the hourly scale (at both 0.1° and 0.25° resolutions), the
567 probability of false alarm is significantly lower for the STREAM ensemble mean than for IMERG
568 (Figure 7). At the hourly scale, the STREAM ensemble mean shows both a higher POD and lower
569 POFA due to the use of the WAR covariate in the pixel-scale CSGD error model (Supplemental
570 Figure S1). By removing the censoring of uniform noise greater than 0.995, the POD of STREAM
571 can be slightly increased for low rain rates at the expense of a slight increase in POFA
572 (Supplemental Figure 2). However, removal of this censoring component in STREAM can lead to
573 ‘INF’ values in the precipitation ensemble when extremely high noise values are ingested by the
574 inverse CDF of conditional distributions. The STREAM ensemble’s ability to bracket ground-
575 reference observations at event and seasonal scales (Figures 5 and 6) suggests that STREAM
576 would be well-suited to creating inputs to hydrologic, land surface, or drought monitoring
577 models—a direction that will be pursued in follow-on work.

578 We reran ensemble generation and analysis using Stage IV in place of IMERG in the
579 correlated noise generation scheme (Figure 3) to understand if applying the ground-reference
580 spatial correlation structure significantly improves ensemble performance; it does not (results not
581 shown). This indicates that IMERG, although imperfect, provides valuable information about error
582 correlation structures, on par with the information available through a ground-reference product.

583 STREAM was run for a 50-member ensemble in this work. Although performance metrics
584 at our data’s native pixel resolution (1-hr, 0.1°) are not impacted by an increase in ensemble size
585 past 25, performance metrics at coarser resolutions (24-hr, 0.25°) improve with increasing
586 ensemble size until a size of roughly 50 (results not shown). This reflects the increasing number
587 of permutations of native resolution errors and error correlation structures that are combined during
588 rescaling to coarser resolutions, leading to a greater range of possible precipitation estimates at
589 coarse resolutions; the implications of this for water resources modeling are unclear and will be
590 explored in future work. It is likely that at resolutions coarser than 24-hr and 0.25° , a larger
591 STREAM ensemble could be beneficial.

592 Although an ensemble-based approach is currently the most feasible way to incorporate
593 precipitation uncertainty into applications that ingest deterministic data, a large number of

594 ensemble members may be required to accurately represent precipitation uncertainty. This may
595 require prohibitive computing resources for the storage of precipitation outputs and the
596 computational demands of hydrologic or land surface models. Although this study does not address
597 this challenge, we note that very little work has been done in attempting to adapt the structure of
598 environmental models to probabilistic precipitation inputs. As summarized in Nogueira (2020),
599 large-scale precipitation estimates involve substantial uncertainties; thus, the adaption of models
600 to ingest probabilistic precipitation data is an appropriate way to account for precipitation
601 uncertainty (e.g. Hartke et al., 2020).

602 6.2 Comparison with SREM2D model

603 The STREAM ensemble meets or exceeds the performance of the SREM2D ensemble at
604 all resolutions and rain rates except for the most extreme hourly rain rates (>10 mm/hr) when
605 SREM2D exhibits a slightly higher containing ratio (Figure 9). SREM2D shows a particularly low
606 containing ratio for light rainfall rates, meaning that SREM2D-perturbed IMERG fields often fail
607 to bracket observed light rainfall rates. Visually, SREM2D fields exhibit more isotropic structure
608 than IMERG, Stage IV, or STREAM ensemble fields (Figure 4). The noticeable drop in CR that
609 occurs when observed rain rate shifts from zero to nonzero (Figure 9) is likely due to the separate
610 handling of rainfall occurrence and hit errors in SREM2D. Even in the presence of plentiful ground
611 data, a climatologically-trained approach to space-time correlation modeling, such as that used in
612 SREM2D, is potentially problematic: each storm system is unique, so properties will deviate from
613 a climatological training. The STREAM approach, in contrast, infers properties directly from each
614 storm and thus foregoes the need for calibration or ground-reference data. STREAM's ability to
615 outperform SREM2D suggests that the use of observed SMP space-time correlation is an attractive
616 and practical alternative to the calibration-based simulation of error correlation.

617 6.3 Comparison with uncorrelated error modeling approach

618 The briefest visual analysis of the uncorrelated ensemble fields reveals that they do not
619 resemble real precipitation, instead exhibiting scattered precipitation and little structure (Figure 4).
620 The mean of the uncorrelated ensemble performs identically to the STREAM ensemble mean
621 (Figure 7) because both ensemble means reflect a bias-corrected version of IMERG, but the range
622 of the STREAM ensemble at coarser resolutions is much greater (compare Supplemental Figure
623 S3 to Figure 5). At coarser space-time scales, the STREAM ensemble incorporates error
624 correlation structures which allow ensemble members to simulate regional over- and
625 underestimation by IMERG, ensuring greater variability among ensemble members. Meanwhile,
626 the uncorrelated ensemble aggregates adjacent pixels with randomly simulated under and over-
627 estimation, averaging out random errors and preventing any simulation of regional over- or
628 underestimation. The uncorrelated ensemble's ability to bracket observed precipitation rates in fact
629 worsens as the ensemble is aggregated to coarser resolutions (Figure 9). The improved
630 performance of STREAM relative to the uncorrelated ensemble emphasizes the central importance
631 of simulating the space-time correlation structure of precipitation error.

632 6.4 STREAM Future Adaptions

633 Although the demonstration of STREAM in this work uses the CSGD error model, other
634 pixel-scale error models, such as PUSH (Maggioni et al., 2014) or PIRSO (Kirstetter et al., 2018)
635 could likely be used within STREAM to represent IMERG uncertainty across arbitrary space-time

636 scales. The CSGD error model is uniquely useful within STREAM, however, due to its ability to
637 incorporate an arbitrary number of covariates to constrain pixel-scale uncertainty estimates.

638 The 850 mb steering winds from MERRA2 that are used here have a latency of several
639 weeks. These data were chosen for illustrative purposes only; steering wind data could be obtained
640 from lower-latency datasets such as from data-assimilating numerical weather forecasts or from
641 the motion vectors used in the IMERG morphing scheme (Tan et al., 2019). This latter option
642 would increase the consistency between how errors propagate over space and time within IMERG
643 and how the correlated noise is propagated in STREAM's semi-Lagrangian advection scheme.
644 This option was not pursued here since the IMERG motion vectors are not publically available;
645 this may be pursued in future work.

646 **7 Conclusions**

647 The potential of satellite multi-sensor precipitation (SMP) products—and other large-scale
648 precipitation sources with similar error/uncertainty properties, such as satellite-assimilating
649 numerical weather models (NWM) and “blended” datasets that combine NWM and SMP data—
650 in water resources modeling is limited by their uncertainties, which can mischaracterize both
651 precipitation occurrence and intensity. Uncertainty during extreme precipitation events is
652 particularly problematic for applications which assess hazards such as flooding or landsliding (e.g.
653 Hartke et al., 2020; Jia et al., 2020; Prakash et al., 2016). Precipitation uncertainty and error vary
654 according to spatial and temporal resolution, with random errors tending to “cancel out” when
655 aggregated in space and time. SMP errors are autocorrelated in space and time, however, leading
656 to regional (i.e. watershed scale) over- or underestimation by satellite-based products. This
657 problem can be remedied using ensemble generation techniques that produce multiple plausible
658 realizations of the unknown true precipitation field conditioned on the SMP observations. To
659 incorporate precipitation uncertainty into applications which consider accumulated precipitation,
660 such as flood prediction or drought monitoring, ensemble members must replicate the space-time
661 correlation structure of precipitation error. This has been called a grand challenge within the
662 precipitation community (Huffman et al., 2019), while the usability of other large-scale
663 precipitation datasets would benefit from breakthroughs.

664 The Space-Time Rainfall Error and Autocorrelation Model (STREAM) combines space-
665 time correlation structures with a pixel scale precipitation error model to generate precipitation
666 ensembles that can “bracket” the magnitude and replicate the correlation structure of higher-
667 accuracy “ground truth” rainfall fields. SMP-based STREAM ensembles are generated at high
668 resolution (1-hour, 0.1°) and are shown to outperform the satellite product IMERG at several
669 spatiotemporal scales. STREAM requires no ground-reference data to run and relies minimally on
670 ground-reference data during calibration. Specifically, the approach taken to model spacetime
671 correlation does not require any ground data and does not even require a “training period,” since
672 all necessary properties are inferred from IMERG and wind fields. STREAM ensembles generated
673 at a high resolution can be aggregated to arbitrary space-time scales for use in hydrologic or land
674 surface models while preserving the characteristics of real precipitation at these scales. The
675 ensemble output of STREAM can be ingested in water modeling applications with no modification
676 to those models' structures. This enables water resource predictions that reflect input precipitation
677 uncertainty, though the computational demands of ensemble simulations may become
678 burdensome.

679 Pixel-scale uncertainty (i.e. the probabilistic uncertainty surrounding a satellite-based
680 precipitation estimate at a single pixel and time step) is the most feasible way to characterize SMP
681 uncertainty around the world. In data-limited regions, pixel-scale precipitation error models can
682 leverage available ground-reference data (i.e. sparse rain gage records), and pixel-scale uncertainty
683 estimates can also be obtained via other approaches (i.e. Kirstetter et al., 2018a; Li et al., 2021).
684 Taken alone, however, pixel scale uncertainty is of limited value in water resources applications
685 because it offers no help in connecting or extending uncertainty estimates to nearby locations in
686 space and time. STREAM allows users to combine pixel-scale precipitation uncertainty in space
687 and time while accounting for nonstationary SMP error correlation structures. While not explored
688 here, it appears that any pixel-scale uncertainty model—and not just the CSGD approach used
689 here—can fit into the STREAM framework.

690 To be applicable to continental-to-global scale applications, a space-time SMP error model
691 must rely minimally or not at all on ground-reference data. STREAM is shown to outperform a
692 previous rainfall error model (SREM2D), which utilized extensive gridded ground-reference data
693 for training SMP error and correlation properties. This work demonstrates that the anisotropic,
694 nonstationary space-time correlation structure of SMP errors can be modeled using only SMP
695 fields and atmospheric motion vectors. Meanwhile, ongoing work has demonstrated that the GPM
696 Dual Precipitation Radar (DPR) instrument, which is quite accurate relative to other space-based
697 microwave and infrared sensors, can be used to train pixel-scale error models (Khan et al., 2018;
698 Li et al., 2021). Combining that approach with STREAM would completely eliminate the need for
699 ground reference data, providing tools that could be used anywhere around the globe—though not
700 without some shortcomings (Z. Li et al., 2021). In addition, the nonstationary and computationally
701 efficient nature of the STREAM ensemble generation means that it could be applied at a global
702 scale. Thus, while challenges remain, we believe that this work constitutes a meaningful step
703 toward solving the grand challenge of characterizing precipitation error across arbitrary space-time
704 scales.

705 **Acknowledgments and Data**

706 S.H. Hartke was supported by the NASA Earth and Space Science Fellowship Program (Award
707 Number 80NSSC18K1321). Z. Li, D.B. Wright, D.B. Kirschbaum, and S. Khan were supported
708 by the NASA Precipitation Measurement Mission (Award Number 80NSSC19K0951). The
709 authors thank Dave Lorenz for providing guidance on space-time correlation structures and semi-
710 Lagrangian schemes, and Danielle Nerini for his guidance in using pysteps noise generation
711 functions. The authors thank Aline Falck for sharing SREM2D calibration and code materials.

712 IMERG-Early and MERRA-2 data is available from NASA's Goddard Earth Sciences Data and
713 Information Services Center (GES DISC) (<https://disc.gsfc.nasa.gov/>). NEXRAD Stage IV data is
714 available from the Earth Observing Laboratory data archive
715 (<https://data.eol.ucar.edu/dataset/21.093>). STREAM code is available via github repository
716 (<https://github.com/sam-hartke/STREAM>).

717

718

719 **References**

- 720 Aghakouchak, A., Behrangi, A., Sorooshian, S., Hsu, K., & Amitai, E. (2011). Evaluation of
721 satellite-retrieved extreme precipitation rates across the central United States. *Journal of*
722 *Geophysical Research Atmospheres*, *116*(2), 1–11. <https://doi.org/10.1029/2010JD014741>
- 723 Alfieri, L., Burek, P., Dutra, E., Krzeminski, B., Muraro, D., Thielen, J., & Pappenberger, F.
724 (2013). GloFAS-global ensemble streamflow forecasting and flood early warning.
725 *Hydrology and Earth System Sciences*, *17*(3), 1161–1175. [https://doi.org/10.5194/hess-17-](https://doi.org/10.5194/hess-17-1161-2013)
726 [1161-2013](https://doi.org/10.5194/hess-17-1161-2013)
- 727 Andresen, J., Hilberg, S., Kunkel, K., Winkler, J., Andresen, J., Hatfield, J., Bidwell, D., &
728 Brown, D. (2012). *Historical Climate and Climate Trends in the Midwestern USA National*
729 *Climate Assessment Midwest Technical Input Report* (Issue U.S. National Climate
730 Assessment Midwest Technical Input Report).
731 http://glisa.msu.edu/docs/NCA/MTIT_Historical.pdf.
- 732 Asong, Z. E., Razavi, S., Wheeler, H. S., & Wong, J. S. (2017). Evaluation of integrated
733 multisatellite retrievals for GPM (IMERG) over Southern Canada against ground
734 precipitation observations: A preliminary assessment. *Journal of Hydrometeorology*, *18*(4),
735 1033–1050. <https://doi.org/10.1175/JHM-D-16-0187.1>
- 736 Beck, H. E., Vergopolan, N., Pan, M., Levizzani, V., Van Dijk, A. I. J. M., Weedon, G. P.,
737 Brocca, L., Pappenberger, F., Huffman, G. J., & Wood, E. F. (2017). Global-scale
738 evaluation of 22 precipitation datasets using gauge observations and hydrological modeling.
739 *Hydrology and Earth System Sciences*, *21*(12), 6201–6217. [https://doi.org/10.5194/hess-21-](https://doi.org/10.5194/hess-21-6201-2017)
740 [6201-2017](https://doi.org/10.5194/hess-21-6201-2017)
- 741 Budikova, D., Coleman, J. S. M. M., Strobe, S. A., & Austin, A. (2010). Hydroclimatology of
742 the 2008 Midwest floods. *Water Resources Research*, *46*(12).
743 <https://doi.org/10.1029/2010WR009206>
- 744 Cuo, L., Pagano, T. C., & Wang, Q. J. (2011). A review of quantitative precipitation forecasts
745 and their use in short- to medium-range streamflow forecasting. *Journal of*
746 *Hydrometeorology*, *12*(5), 713–728. <https://doi.org/10.1175/2011JHM1347.1>
- 747 Falck, A. S., Maggioni, V., Tomasella, J., Vila, D. A., & Diniz, F. L. R. (2015). Propagation of
748 satellite precipitation uncertainties through a distributed hydrologic model: A case study in
749 the Tocantins-Araguaia basin in Brazil. *Journal of Hydrology*, *527*, 943–957.
750 <https://doi.org/10.1016/j.jhydrol.2015.05.042>
- 751 Franz, K. J., & Hogue, T. S. (2011). Evaluating uncertainty estimates in hydrologic models:
752 Borrowing measures from the forecast verification community. *Hydrology and Earth*
753 *System Sciences*, *15*(11), 3367–3382. <https://doi.org/10.5194/hess-15-3367-2011>
- 754 Funk, C., Shukla, S., Thiaw, W. M., Rowland, J., Hoell, A., McNally, A., Husak, G., Novella, N.,
755 Budde, M., Peters-Lidard, C., Adoum, A., Galu, G., Korecha, D., Magadzire, T., Rodriguez,
756 M., Robjhon, M., Bekele, E., Arsenault, K., Peterson, P., ... Verdin, J. (2019). Recognizing
757 the famine early warning systems network over 30 years of drought early warning science
758 advances and partnerships promoting global food security. *Bulletin of the American*
759 *Meteorological Society*, *100*(6), 1011–1027. <https://doi.org/10.1175/BAMS-D-17-0233.1>
- 760 Gadelha, A. N., Coelho, V. H. R., Xavier, A. C., Barbosa, L. R., Melo, D. C. D., Xuan, Y.,

- 761 Huffman, G. J., Petersen, W. A., & Almeida, C. das N. (2019). Grid box-level evaluation of
762 IMERG over Brazil at various space and time scales. *Atmospheric Research*, 218(October
763 2018), 231–244. <https://doi.org/10.1016/j.atmosres.2018.12.001>
- 764 Gebregiorgis, A. S., Kirstetter, P. E., Hong, Y. E., Gourley, J. J., Huffman, G. J., Petersen, W.
765 A., Xue, X., & Schwaller, M. R. (2018). To What Extent is the Day 1 GPM IMERG
766 Satellite Precipitation Estimate Improved as Compared to TRMM TMPA-RT? *Journal of*
767 *Geophysical Research: Atmospheres*, 123(3), 1694–1707.
768 <https://doi.org/10.1002/2017JD027606>
- 769 Gebremichael, M., Liao, G. Y., & Yan, J. (2011). Nonparametric error model for a high
770 resolution satellite rainfall product. *Water Resources Research*, 47(7), 7504.
771 <https://doi.org/10.1029/2010WR009667>
- 772 Gelaro, R., McCarty, W., Suárez, M. J., Todling, R., Molod, A., Takacs, L., Randles, C. A.,
773 Darmenov, A., Bosilovich, M. G., Reichle, R., Wargan, K., Coy, L., Cullather, R., Draper,
774 C., Akella, S., Buchard, V., Conaty, A., da Silva, A. M., Gu, W., ... Zhao, B. (2017). The
775 modern-era retrospective analysis for research and applications, version 2 (MERRA-2).
776 *Journal of Climate*, 30(14), 5419–5454. <https://doi.org/10.1175/JCLI-D-16-0758.1>
- 777 Germann, U., & Zawadzki, I. (2002). Scale-dependence of the predictability of precipitation
778 from continental radar images. Part I: Description of the methodology. *Monthly Weather*
779 *Review*, 130(12), 2859–2873. [https://doi.org/10.1175/1520-
780 0493\(2002\)130<2859:SDOTPO>2.0.CO;2](https://doi.org/10.1175/1520-0493(2002)130<2859:SDOTPO>2.0.CO;2)
- 781 Gottschalck, J., Meng, J., Rodell, M., & Houser, P. (2005). Analysis of multiple precipitation
782 products and preliminary assessment of their impact on Global Land Data Assimilation
783 System land surface states. *Journal of Hydrometeorology*, 6(5), 573–598.
784 <https://doi.org/10.1175/JHM437.1>
- 785 Hartke, S. H., Wright, D. B., Kirschbaum, D. B., Stanley, T. A., & Li, Z. (2020). Incorporation
786 of satellite precipitation uncertainty in a landslide hazard nowcasting system. *Journal of*
787 *Hydrometeorology*, 21(8), 1741–1759. <https://doi.org/10.1175/JHM-D-19-0295.1>
- 788 Hossain, F., & Anagnostou, E. N. (2005). Numerical investigation of the impact of uncertainties
789 in satellite rainfall estimation and land surface model parameters on simulation of soil
790 moisture. *Advances in Water Resources*, 28(12), 1336–1350.
791 <https://doi.org/10.1016/j.advwatres.2005.03.013>
- 792 Hossain, F., & Anagnostou, E. N. (2006). A two-dimensional satellite rainfall error model. *IEEE*
793 *Transactions on Geoscience and Remote Sensing*, 44(6), 1511–1522.
794 <https://doi.org/10.1109/TGRS.2005.863866>
- 795 Hossain, F., Anagnostou, E. N., & Dinku, T. (2004). Sensitivity analyses of satellite rainfall
796 retrieval and sampling error on flood prediction uncertainty. *IEEE Transactions on*
797 *Geoscience and Remote Sensing*, 42(1), 130–139.
798 <https://doi.org/10.1109/TGRS.2003.818341>
- 799 Huffman, G., Bolvin, D. T., Braithwaite, D., Hsu, K., Joyce, R., Kidd, C., Nelkin, E. J.,
800 Sorooshian, S., Tan, J., & Xie, P. (2019). NASA Global Precipitation Measurement (GPM)
801 Integrated Multi-satellitE Retrievals for GPM (IMERG) Prepared for: Global Precipitation
802 Measurement (GPM) National Aeronautics and Space Administration (NASA). In

- 803 *Algorithm Theoretical Basis Document (ATBD) Version 06* (Issue March).
804 https://pmm.nasa.gov/sites/default/files/imce/times_allsat.jpg
- 805 Jia, G., Tang, Q., & Xu, I. X. (2020). Evaluating the performances of satellite-based rainfall data
806 for global rainfall-induced landslide warnings. *Landslides*, 17, 283.
807 <https://doi.org/10.1007/s10346-019-01277-6>
- 808 Khan, S., & Maggioni, V. (2020). Evaluating the Applicability of the PUSH Framework to
809 Quasi-Global Infrared Precipitation Retrievals at 0.5°/Daily Spatial/Temporal Resolution.
810 *Asia-Pacific Journal of Atmospheric Sciences*. <https://doi.org/10.1007/s13143-020-00185-3>
- 811 Khan, S., Maggioni, V., & Kirstetter, P. E. (2018). Investigating the Potential of Using Satellite-
812 Based Precipitation Radars as Reference for Evaluating Multisatellite Merged Products.
813 *Journal of Geophysical Research: Atmospheres*, 123(16), 8646–8660.
814 <https://doi.org/10.1029/2018JD028584>
- 815 Kidd, C., Becker, A., Huffman, G. J., Muller, C. L., Joe, P., Skofronick-Jackson, G., &
816 Kirschbaum, D. B. (2017). So, how much of the Earth's surface is covered by rain gauges?
817 *Bulletin of the American Meteorological Society*, 98(1), 69–78.
818 <https://doi.org/10.1175/BAMS-D-14-00283.1>
- 819 Kirschbaum, D., & Stanley, T. (2018). Satellite-Based Assessment of Rainfall-Triggered
820 Landslide Hazard for Situational Awareness. *Earth's Future*, 6(3), 505–523.
821 <https://doi.org/10.1002/2017EF000715>
- 822 Kirstetter, P. E., Karbalaee, N., Hsu, K., & Hong, Y. (2018). Probabilistic precipitation rate
823 estimates with space-based infrared sensors. *Quarterly Journal of the Royal Meteorological*
824 *Society*, 144(December 2017), 191–205. <https://doi.org/10.1002/qj.3243>
- 825 Kirstetter, P., Karbalaee, N., Hsu, K., & Hong, Y. (2018). Probabilistic precipitation rate
826 estimates with space-based infrared sensors. *Quarterly Journal of the Royal Meteorological*
827 *Society*, 144(S1), 191–205. <https://doi.org/10.1002/qj.3243>
- 828 Lauritzen, P. H., Jablonowski, C., Taylor, M. A., & Nai, R. D. (2011). Atmospheric Transport
829 Schemes: Desirable Properties and a Semi-Lagrangian View on Finite-Volume
830 Discretizations. In *Numerical Techniques for Global Atmospheric Models* (pp. 185–250).
831 Springer Berlin / Heidelberg.
- 832 Li, N., Tang, G., Zhao, P., Hong, Y., Gou, Y., & Yang, K. (2016). *Statistical assessment and*
833 *hydrological utility of the latest multi-satellite precipitation analysis IMERG in Ganjiang*
834 *River basin*. <https://doi.org/10.1016/j.atmosres.2016.07.020>
- 835 Li, Z., Wright, D., Hartke, S., Kirschbaum, D., Khan, S., Maggioni, V., & Kirstetter, P.-E.
836 (2021). Toward A Globally-Applicable Uncertainty Quantification Framework for Satellite
837 Multisensor Precipitation Products based on GPM DPR. *Earth and Space Science Open*
838 *Archive*. <https://doi.org/10.1002/ESSOAR.10507263.1>
- 839 Lin, Y., *GCIP/EOP Surface: Precipitation NCEP/EMC 4KM Gridded Data (GRIB) Stage IV*
840 *Data. Version 1.0*, (2011) (testimony of Y. Lin). <https://data.eol.ucar.edu/dataset/21.093>
- 841 Maggioni, V., Meyers, P. C., & Robinson, M. D. (2016). A review of merged high-resolution
842 satellite precipitation product accuracy during the Tropical Rainfall Measuring Mission
843 (TRMM) era. In *Journal of Hydrometeorology* (Vol. 17, Issue 4, pp. 1101–1117).

- 844 <https://doi.org/10.1175/JHM-D-15-0190.1>
- 845 Maggioni, V., Reichle, R. H., & Anagnostou, E. N. (2011). The effect of satellite rainfall error
846 modeling on soil moisture prediction uncertainty. *Journal of Hydrometeorology*, *12*(3),
847 413–428. <https://doi.org/10.1175/2011JHM1355.1>
- 848 Maggioni, V., Sapiano, M. R. P., Adler, R. F., Tian, Y., & Huffman, G. J. (2014). An Error
849 Model for Uncertainty Quantification in High-Time-Resolution Precipitation Products.
850 *Journal of Hydrometeorology*, *15*(3), 1274–1292. <https://doi.org/10.1175/jhm-d-13-0112.1>
- 851 Maggioni, V., Vergara, H. J., Anagnostou, E. N., Gourley, J. J., Hong, Y., & Stampoulis, D.
852 (2013). Investigating the Applicability of Error Correction Ensembles of Satellite Rainfall
853 Products in River Flow Simulations. *Journal of Hydrometeorology*, *14*(4), 1194–1211.
854 <https://doi.org/10.1175/jhm-d-12-074.1>
- 855 Mantoglou, A., & Wilson, J. L. (1982). The Turning Bands Method for simulation of random
856 fields using line generation by a spectral method. *Water Resources Research*, *18*(5), 1379–
857 1394. <https://doi.org/10.1029/WR018i005p01379>
- 858 Najibi, N., Devineni, N., & Lu, M. (2016). *Hydroclimate Drivers and Atmospheric*
859 *Teleconnections of Long Duration Floods: An Application to Large Reservoirs in the*
860 *Missouri River Basin*. <http://www.elsevier.com/open-access/userlicense/1.0/2>
- 861 Nakamura, J., Lall, U., Kushnir, Y., Robertson, A. W., & Seager, R. (2013). Dynamical structure
862 of extreme floods in the U.S. Midwest and the United Kingdom. *Journal of*
863 *Hydrometeorology*, *14*(2), 485–504. <https://doi.org/10.1175/JHM-D-12-059.1>
- 864 Nerini, D., Besic, N., Sideris, I., Germann, U., & Foresti, L. (2017). A non-stationary stochastic
865 ensemble generator for radar rainfall fields based on the short-space Fourier transform.
866 *Hydrology and Earth System Sciences*, *21*(6), 2777–2797. [https://doi.org/10.5194/hess-21-](https://doi.org/10.5194/hess-21-2777-2017)
867 [2777-2017](https://doi.org/10.5194/hess-21-2777-2017)
- 868 Niemi, T. J., Kokkonen, T., & Seed, A. W. (2014). A simple and effective method for
869 quantifying spatial anisotropy of time series of precipitation fields. *Water Resources*
870 *Research*, *50*(7), 5906–5925. <https://doi.org/10.1002/2013WR015190>
- 871 Nijssen, B., & Lettenmaier, D. P. (2004). Effect of precipitation sampling error on simulated
872 hydrological fluxes and states: Anticipating the Global Precipitation Measurement satellites.
873 *Journal of Geophysical Research D: Atmospheres*, *109*(2), 1–15.
874 <https://doi.org/10.1029/2003jd003497>
- 875 Nikolopoulos, E. I., Anagnostou, E. N., Hossain, F., Gebremichael, M., & Borga, M. (2010).
876 Understanding the scale relationships of uncertainty propagation of satellite rainfall through
877 a distributed hydrologic model. *Journal of Hydrometeorology*, *11*(2), 520–532.
878 <https://doi.org/10.1175/2009JHM1169.1>
- 879 Nogueira, M. (2020). Inter-comparison of ERA-5, ERA-interim and GPCP rainfall over the last
880 40 years: Process-based analysis of systematic and random differences. *Journal of*
881 *Hydrology*, *583*. <https://doi.org/10.1016/j.jhydrol.2020.124632>
- 882 Prakash, S., Mitra, A. K., Pai, D. S., & AghaKouchak, A. (2016). From TRMM to GPM: How
883 well can heavy rainfall be detected from space? *Advances in Water Resources*,
884 *88*(December 2014), 1–7. <https://doi.org/10.1016/j.advwatres.2015.11.008>

- 885 Prince, S. D., Haskett, J., Steininger, M., Strand, H., & Wright, R. (2001). Net primary
886 production of U.S. midwest croplands from agricultural harvest yield data. *Ecological*
887 *Applications*, *11*(4), 1194–1205. [https://doi.org/10.1890/1051-](https://doi.org/10.1890/1051-0761(2001)011[1194:NPPOUS]2.0.CO;2)
888 [0761\(2001\)011\[1194:NPPOUS\]2.0.CO;2](https://doi.org/10.1890/1051-0761(2001)011[1194:NPPOUS]2.0.CO;2)
- 889 Pulkkinen, S., Nerini, D., Pérez Hortal, A. A., Velasco-Forero, C., Seed, A., Germann, U., &
890 Foresti, L. (2019). Pysteps: An open-source Python library for probabilistic precipitation
891 nowcasting (v1.0). *Geoscientific Model Development*, *12*(10), 4185–4219.
892 <https://doi.org/10.5194/gmd-12-4185-2019>
- 893 Quintero, F., Krajewski, W. F., Mantilla, R., Small, S., & Seo, B. C. (2016). A spatial-dynamical
894 framework for evaluation of satellite rainfall products for flood prediction. *Journal of*
895 *Hydrometeorology*, *17*(8), 2137–2154. <https://doi.org/10.1175/JHM-D-15-0195.1>
- 896 Reichle, R. H., Koster, R. D., Liu, P., Mahanama, S. P. P., Njoku, E. G., & Owe, M. (2007).
897 Comparison and assimilation of global soil moisture retrievals from the Advanced
898 Microwave Scanning Radiometer for the Earth Observing System (AMSR-E) and the
899 Scanning Multichannel Microwave Radiometer (SMMR). *Journal of Geophysical Research*
900 *Atmospheres*, *112*(9). <https://doi.org/10.1029/2006JD008033>
- 901 Rodell, B. Y. M., Houser, P. R., Jambor, U., Gottschalck, J., Mitchell, K., Meng, C., Arsenault,
902 K., Cosgrove, B., Radakovich, J., Bosilovich, M., Entin, J. K., Walker, J. P., Lohmann, D.,
903 & Toll, D. (2004). THE GLOBAL LAND DATA ASSIMILATION SYSTEM. *Bull. Amer.*
904 *Meteor. Soc.*, *85*(3), 381–394. <https://doi.org/10.1175/BAMS-85-3-381>
- 905 Sarachi, S., Hsu, K., & Sorooshian, S. (2015). A Statistical Model for the Uncertainty Analysis
906 of Satellite Precipitation Products. *Journal of Hydrometeorology*, *16*(5), 2101–2117.
907 <https://doi.org/10.1175/jhm-d-15-0028.1>
- 908 Scheuerer, M., & Hamill, T. M. (2015). Statistical Postprocessing of Ensemble Precipitation
909 Forecasts by Fitting Censored, Shifted Gamma Distributions*. *Monthly Weather Review*.
910 <https://doi.org/10.1175/MWR-D-15-0061.1>
- 911 Schreiner-McGraw, A. P., & Ajami, H. (2020). Impact of Uncertainty in Precipitation Forcing
912 Data Sets on the Hydrologic Budget of an Integrated Hydrologic Model in Mountainous
913 Terrain. *Water Resources Research*, *56*(12). <https://doi.org/10.1029/2020WR027639>
- 914 Serpetzoglou, E., Anagnostou, E. N., Papadopoulos, A., Nikolopoulos, E. I., & Maggioni, V.
915 (2010). Error propagation of remote sensing rainfall estimates in soil moisture prediction
916 from a land surface model. *Journal of Hydrometeorology*, *11*(3), 705–720.
917 <https://doi.org/10.1175/2009JHM1166.1>
- 918 Shige, S., Kida, S., Ashiwake, H., Kubota, T., & Aonashi, K. (2013). Improvement of TMI rain
919 retrievals in mountainous areas. *Journal of Applied Meteorology and Climatology*, *52*(1),
920 242–254. <https://doi.org/10.1175/JAMC-D-12-074.1>
- 921 Shrestha, A., Nair, A. S., & Indu, J. (2020). Role of precipitation forcing on the uncertainty of
922 land surface model simulated soil moisture estimates. *Journal of Hydrology*, *580*(February
923 2019), 124264. <https://doi.org/10.1016/j.jhydrol.2019.124264>
- 924 Smith, J. A., Baeck, M. L., Villarini, G., Wright, D. B., & Krajewski, W. (2013). Extreme flood
925 response: The June 2008 flooding in Iowa. *Journal of Hydrometeorology*, *14*(6), 1810–
926 1825. <https://doi.org/10.1175/JHM-D-12-0191.1>

- 927 Staniforth, A., & Cote, J. (1991). Semi-Lagrangian integration schemes for atmospheric models -
928 a review. *Monthly Weather Review*, *119*(9), 2206–2223. [https://doi.org/10.1175/1520-0493\(1991\)119<2206:SLISFA>2.0.CO;2](https://doi.org/10.1175/1520-0493(1991)119<2206:SLISFA>2.0.CO;2)
- 930 Sun, Q., Miao, C., Duan, Q., Ashouri, H., Sorooshian, S., & Hsu, K. L. (2018). A Review of
931 Global Precipitation Data Sets: Data Sources, Estimation, and Intercomparisons. *Reviews of*
932 *Geophysics*, *56*(1), 79–107. <https://doi.org/10.1002/2017RG000574>
- 933 Tan, J., Huffman, G. J., Bolvin, D. T., & Nelkin, E. J. (2019). IMERG V06: Changes to the
934 morphing algorithm. *Journal of Atmospheric and Oceanic Technology*, *36*(12), 2471–2482.
935 <https://doi.org/10.1175/JTECH-D-19-0114.1>
- 936 Tan, J., Petersen, W. A., Kirchengast, G., Goodrich, D. C., & Wolff, D. B. (2018). Evaluation of
937 global precipitation measurement rainfall estimates against three dense gauge networks.
938 *Journal of Hydrometeorology*, *19*(3), 517–532. <https://doi.org/10.1175/JHM-D-17-0174.1>
- 939 Tan, J., Petersen, W., & Tokay, A. (2016). A Novel Approach to Identify Sources of Errors in
940 IMERG for GPM Ground Validation. *Journal of Hydrometeorology*, *17*(9), 2477–2491.
941 <https://doi.org/10.1175/JHM-D-16-0079.s1>
- 942 Tang, G., Clark, M. P., Papalexiou, S. M., Ma, Z., & Hong, Y. (2020). Have satellite
943 precipitation products improved over last two decades? A comprehensive comparison of
944 GPM IMERG with nine satellite and reanalysis datasets. *Remote Sensing of Environment*,
945 *240*(January). <https://doi.org/10.1016/j.rse.2020.111697>
- 946 Tang, G., Ma, Y., Long, D., Zhong, L., & Hong, Y. (2016). Evaluation of GPM Day-1 IMERG
947 and TMPA Version-7 legacy products over Mainland China at multiple spatiotemporal
948 scales. *Journal of Hydrology*, *533*, 152–167. <https://doi.org/10.1016/j.jhydrol.2015.12.008>
- 949 Tian, Y., & Peters-Lidard, C. D. (2007). Systematic anomalies over inland water bodies in
950 satellite-based precipitation estimates. *Geophysical Research Letters*, *34*(14), 1–5.
951 <https://doi.org/10.1029/2007GL030787>
- 952 Tian, Y., & Peters-Lidard, C. D. (2010). A global map of uncertainties in satellite-based
953 precipitation measurements. *Geophysical Research Letters*, *37*(24), 1–6.
954 <https://doi.org/10.1029/2010GL046008>
- 955 Tian, Y., Peters-Lidard, C. D., Eylander, J. B., Joyce, R. J., Huffman, G. J., Adler, R. F., Hsu, K.
956 L., Turk, F. J., Garcia, M., & Zeng, J. (2009). Component analysis of errors in Satellite-
957 based precipitation estimates. *Journal of Geophysical Research Atmospheres*, *114*(24), 1–
958 15. <https://doi.org/10.1029/2009JD011949>
- 959 Villarini, G., Krajewski, W. F., Ciach, G. J., & Zimmerman, D. L. (2009). Product-error-driven
960 generator of probable rainfall conditioned on WSR-88D precipitation estimates. *Water*
961 *Resources Research*, *45*(1), 1–11. <https://doi.org/10.1029/2008WR006946>
- 962 Winiwarter, V., Haidvogel, G., & Bürkner, M. (2016). The rise and fall of Munich's early modern
963 water network: a tale of prowess and power. *Water History*, *8*(3), 277–299.
964 <https://doi.org/10.1007/s12685-016-0173-y>
- 965 Wright, D. B. (2018). Rainfall Information for Global Flood Modeling. In G. Schumann, P. D.
966 Bates, H. Apel, & G. T. Aronica (Eds.), *Global Flood Hazard: Applications in Modeling,*
967 *Mapping, and Forecasting* (pp. 19–42). John Wiley & Sons, Inc. and American

968 Geophysical Union.

969 Wright, D. B., Kirschbaum, D. B., & Yatheendradas, S. (2017). Satellite Precipitation
970 Characterization, Error Modeling, and Error Correction Using Censored Shifted Gamma
971 Distributions. *Journal of Hydrometeorology*, 18(10), 2801–2815.
972 <https://doi.org/10.1175/JHM-D-17-0060.1>

973 Wu, H., Adler, R. F., Tian, Y., Huffman, G. J., Li, H., & Wang, J. (2014). Real-time global flood
974 estimation using satellite-based precipitation and a coupled land surface and routing model.
975 *Water Resources Research*, 50(3), 2693–2717. <https://doi.org/10.1002/2013WR014710>

976 Xiong, L., & O’Connor, K. M. (2008). An empirical method to improve the prediction limits of
977 the GLUE methodology in rainfall-runoff modeling. *Journal of Hydrology*, 349(1–2), 115–
978 124. <https://doi.org/10.1016/j.jhydrol.2007.10.029>

979 Zawadzki, I. I. (1973). Statistical Properties of Precipitation Patterns. *Journal of Applied*
980 *Meteorology and Climatology*, 12(3), 459–472. [https://doi.org/https://doi.org/10.1175/1520-0450\(1973\)012<0459:SPOPP>2.0.CO;2](https://doi.org/https://doi.org/10.1175/1520-0450(1973)012<0459:SPOPP>2.0.CO;2)

982

983